Biochemical and Biophysical Research Communications 443 (2014) 808–813

Contents lists available at ScienceDirect

Biochemical and Biophysical Research Communications

journal homepage: www.elsevier.com/locate/ybbrc

Evaluation and identification of hepatitis B virus entry inhibitors using HepG2 cells overexpressing a membrane transporter NTCP ☆

Masashi Iwamoto [a,b], Koichi Watashi [a,b,*], Senko Tsukuda [a,c], Hussein Hassan Aly [a], Masayoshi Fukasawa [d], Akira Fujimoto [a], Ryosuke Suzuki [a], Hideki Aizaki [a], Takayoshi Ito [e], Osamu Koiwai [b], Hiroyuki Kusuhara [f], Takaji Wakita [a]

[a] Department of Virology II, National Institute of Infectious Diseases, Tokyo 162-8640, Japan
[b] Department of Applied Biological Science, Tokyo University of Sciences, Noda 278-8510, Japan
[c] Micro-signaling Regulation Technology Unit, RIKEN Center for Life Science Technologies, Wako 351-0198, Japan
[d] Department of Biochemistry and Cell Biology, National Institute of Infectious Diseases, Tokyo 162-8640, Japan
[e] Division of Gastroenterology, Department of Medicine, Showa University School of Medicine, Tokyo 142-8666, Japan
[f] The University of Tokyo, Graduate School of Pharmaceutical Sciences, Tokyo 113-0033, Japan

ARTICLE INFO

Article history:
Received 24 November 2013
Available online 14 December 2013

Keywords:
HBV
Infection
NTCP
DMSO
Cyclosporin
Oxysterol

ABSTRACT

Hepatitis B virus (HBV) entry has been analyzed using infection-susceptible cells, including primary human hepatocytes, primary tupaia hepatocytes, and HepaRG cells. Recently, the sodium taurocholate cotransporting polypeptide (NTCP) membrane transporter was reported as an HBV entry receptor. In this study, we established a strain of HepG2 cells engineered to overexpress the human NTCP gene (HepG2-hNTCP-C4 cells). HepG2-hNTCP-C4 cells were shown to be susceptible to infection by blood–borne and cell culture-derived HBV. HBV infection was facilitated by pretreating cells with 3% dimethyl sulfoxide permitting nearly 50% of the cells to be infected with HBV. Knockdown analysis suggested that HBV infection of HepG2-hNTCP-C4 cells was mediated by NTCP. HBV infection was blocked by an anti-HBV surface protein neutralizing antibody, by compounds known to inhibit NTCP transporter activity, and by cyclosporin A and its derivatives. The infection assay suggested that cyclosporin B was a more potent inhibitor of HBV entry than was cyclosporin A. Further chemical screening identified oxysterols, oxidized derivatives of cholesterol, as inhibitors of HBV infection. Thus, the HepG2-hNTCP-C4 cell line established in this study is a useful tool for the identification of inhibitors of HBV infection as well as for the analysis of the molecular mechanisms of HBV infection.

1. Introduction

Approximately 350 million people are estimated to be infected with hepatitis B virus (HBV) worldwide [1–4]. Chronically infected patients are at a greater risk of developing hepatocellular carcinoma. Currently, clinical treatment for HBV infection includes interferon (IFN)α and nucleos(t)ide analogs [2,4]. IFNα therapy yields long-term clinical benefit in less than 40% of the treated patients and can cause significant side effects. Nucleos(t)ide analog treatment can suppress HBV replication with substantial biochemical and histological improvement; however, such analogs may select drug-resistant viruses, thereby limiting the efficacy of long-term treatment. Thus, the development of new anti-HBV agents targeting a different molecule in the HBV life cycle is urgently needed.

HBV is a hepatotropic virus that mainly or exclusively infects human liver [1,5]. HBV infection can be reproduced in cell culture using primary human hepatocytes (PHH), primary tupaia hepatocytes (PTH), and HepaRG cells [6]. Although HBV infection into these cells is robust, these models have significant limitations as tools for analyzing the mechanisms of HBV infection. Notably, these models can yield unstable reproducibility among lots and low tolerability of transfection efficiency with plasmid and siRNA: preparation and culturing of these cells require significant

Abbreviations: Ab, antibody; cccDNA, covalently closed circular DNA; Cs, cyclosporin; DMSO, dimethyl sulfoxide; GEq, genome equivalent; HBc, HBV core protein; HBs, HBV surface protein; HBV, hepatitis B virus; NTCP, sodium taurocholate cotransporting polypeptide; OHC, hydroxycholesterol; PHH, primary human hepatocytes; PTH, primary tupaia hepatocytes.

* Corresponding author at: Department of Virology II, National Institute of Infectious Diseases, 1-23-1 Toyama, Shinjuku-ku, Tokyo 162-8640, Japan. Fax: +81 3 5285 1161.
E-mail address: kwatashi@nih.go.jp (K. Watashi).

0006-291X/$ - see front matter © 2013 The Authors. Published by Elsevier Inc. All rights reserved.
http://dx.doi.org/10.1016/j.bbrc.2013.12.052

technical skill. In the case of hepatitis C virus (HCV), development of the HCV cell culture (HCVcc) system, in which HCV produced from a JFH-1 strain-based molecular clone can reinfect Huh-7 cells, greatly contribute to the characterization of the HCV life cycle and the evaluation of novel anti-HCV drug candidates [7]. However, the above-noted limitations of HBV-susceptible cells have hampered analysis of the HBV life cycle and impeded identification of new anti-HBV drug targets. Thus, establishment of a novel cell line supporting HBV infection is expected to accelerate the molecular analyses of HBV infection as well as the development of anti-HBV agents.

Recently, the sodium taurocholate cotransporting polypeptide (NTCP) membrane transporter was reported as an HBV entry receptor [8]. NTCP is a sodium-dependent transporter for taurocholic acid, and belongs to a family of solute carrier proteins that consist of seven members (SLC10A1-A7) [9,10]. NTCP is expressed at the basolateral membrane of hepatocytes and mediates the transport of conjugated bile acids and some drugs from portal blood to the liver [11]. NTCP specifically interacts with the large surface protein of HBV, thereby functioning as a viral entry receptor [8].

In this study, we established a strain of HepG2 cells engineered to overexpress the NTCP-encoding gene. One of these clones, designated HepG2-hNTCP-C4, was shown to be highly susceptible for HBV infection, confirming that this infection is mediated by NTCP and permitting evaluation in these cells of the anti-HBV activity of various compounds: reduction of HBV infection of HepG2-hNTCP-C4 cells was observed upon treatment with compounds that blocked HBV entry in other assays and by known inhibitors of NTCP transporter activity [12]. A small-scale chemical screen permitted use to identify oxysterols as inhibitors of HBV infection. Thus, the cell line established in this study is useful for screening for anti-HBV agents, as well as for analysis of the molecular mechanisms of HBV infection.

2. Materials and methods

2.1. Reagents

Dimethyl sulfoxide (DMSO), anti-FLAG antibody (Ab), dextran sulfate, cholate, progesterone, 22(S)-hydroxycholesterol (OHC), 25-OHC, 20α-OHC, and 7β-OHC were purchased from Sigma. Ursodeoxycholate was purchased from Tokyo Chemical Industry. Bromosulfophthalein was from MP biomedicals. Cyclosporin (Cs)A, CsB, CsC, CsD, and CsH were obtained from Enzo Lifesciences. Anti-HBV surface protein (HBs) Ab was from Abcam. Heparin was obtained from Mochida Pharmaceuticals. Myrcludex-B was kindly provided by Dr. Stephan Urban at University Hospital Heidelberg and was synthesized by CS Bio (Shanghai, China).

2.2. Cell culture and plasmid transfection

HepG2 and HepG2-hNTCP-C4 cells were cultured with DMEM/F-12 + GlutaMax (Invitrogen) supplemented with 10 mM HEPES (Invitrogen), 200 units/ml penicillin, 200 μg/ml streptomycin, 10% FBS, 50 μM hydrocortisone and 5 μg/ml insulin in the presence (HepG2-hNTCP-C4 cells) or absence (HepG2 cells) of 400 μg/ml G418 (Nacalai). HepAD38 (kindly provided by Dr. Christoph Seeger at Fox Chase Cancer Center) [13] and HepaRG cells (BIOPREDIC) were cultured as described previously [14].

An expression plasmid for hNTCP [15] was transfected into HepG2 cells with TransIT-LT1 (Mirus) according to the manufacturer's instruction to establish HepG2-hNTCP-C4 cells.

2.3. HBV preparation and infection

HBV was prepared and infected as described [14]. Except as noted, the HBV used in this study was genotype D derived from HepAD38 cells [13]. HBV was infected into NTCP-expressing HepG2 cells at 6×10^3 or 1.8×10^4 genome equivalent (GEq)/cell or into HepaRG cells at 6×10^3 GEq/cell. All infections were performed in the presence of 4% PEG8000 at 37 °C for 16 h as previously described [14]. Dr. Urban's group reported that a quantity of more than 10^4 GEq/cell (i.e. $1.25 - 40 \times 10^4$ GEq/cell) of HBV derived from HepAD38 or HepG2.2.15 cells was required as an inoculum for efficient infection into HepaRG cells in the presence of 4% PEG8000 [16]. A limited number of infections were performed with HBV of genotype C, derived from the serum of an HBV-infected patient, at 100 GEq/cell.

2.4. Real-time PCR and RT-PCR

Real-time PCR for quantification of HBV covalently closed circular (ccc)DNA were performed as described [14]. Isolation of total RNA from cell lysates and reverse transcription PCR (RT-PCR) using a One step RNA PCR kit (Takara) were performed as described previously [17]. Primers used in this study were as follows: 5′-AGGGAGGAGGTGGCAATCAAGAGTGG-3′ and 5′-CCGGCTGAAGAACATTGAGGCACTGG-3′ for NTCP, 5′-CCATGGAGAAGGCTGGGG-3′ and 5′-CAAAGTTGTCATGGATGACC-3′ for GAPDH, respectively.

2.5. Detection of HBs and HBe antigens

HBs antigen was quantified by ELISA as described previously [14]. HBe antigen was detected by Chemiluminescent Immuno Assay (Mitsubishi Chemical Medience).

2.6. Southern blot analysis

Isolation of cellular DNA and southern blot analysis to detect HBV DNAs were performed as described previously [14].

2.7. Indirect immunofluorescence analysis

Immunofluorescence was conducted essentially as described [14] using an anti-HBc Ab (#B0586, DAKO) at a dilution of 1:1000.

2.8. Flow cytometry

An aliquot of 1×10^6 of HepG2 or HepG2-hNTCP-C4 cells was incubated for 30 min with a 1:50 dilution of anti-NTCP Ab (Abcam), then washed and incubated with a dye-labeled secondary Ab (Alexa Fluor 488, Invitrogen) at 1:500 dilution in the dark. Staining and washing were carried out at 4 °C in PBS supplemented with 0.5% bovine serum albumin and 0.1% sodium azide. The signals were analyzed with Cell Sorter SH8000 (SONY).

2.9. siRNA transfection

siRNAs were transfected into the cells at a final concentration of 10–30 nM using Lipofectamine RNAiMAX (Invitrogen) according to the manufacturer's protocol. siRNAs were purchased from Sigma.

2.10. Statistical analyses

Statistical analyses are done with student *t*-test.

3. Results and discussion

3.1. Establishment of a cell line susceptible to HBV infection

To establish a cell line permanently expressing NTCP, we transfected an NTCP-encoding plasmid into HepG2 cells and selected with G418 at 1 mg/ml for 3 weeks. The resultant 9 cell clones were isolated and NTCP expression was analyzed by RT-PCR. One of these clones, designated HepG2-hNTCP-C4, was used in the following experiments because this specific clone exhibited high expression of NTCP and high susceptibility to HBV infection, as shown below. Specifically, NTCP mRNA was abundantly expressed in HepG2-hNTCP-C4 cells, in contrast to little to no expression of NTCP mRNA in the parental HepG2 cells (Fig. 1A). Consistent with the mRNA levels, NTCP protein was detected on the cell surface in HepG2-hNTCP-C4 cells (Fig. 1B). To evaluate HBV infection, these cells were inoculated with HBV for 16 h and cultured in normal growth medium for an additional 12 days, and then HBV surface protein (HBs) and HBe antigens in the culture supernatant as well as HBV DNAs, covalently closed circular (ccc)DNA, and HBV core (HBc) in the cells were assessed. The HBV inoculum used in this experiment was of genotype D, and was derived from the culture supernatant of HepAD38 cells that produce HBV by depletion of tetracycline [13]. To confirm that the detected signals were derived from HBV infection and did not represent non-specific background, the cells were incubated with 1 μM Myrcludex-B (or with DMSO vehicle) for 3 h prior to and for 16 h during HBV infection. Myrcludex-B is a lipopeptide consisting of amino acid residues 2–48 of the pre-S1 region of HBV, and is known to block HBV entry [18]. Following HBV exposure, little or no HBs and HBe antigens was detected in the culture supernatant of the parental HepG2 cells, and little HBc protein was observed in these cells (Fig. 1C, D, and G). However, these proteins, as well as HBV DNAs and cccDNA, were detected in HBV-treated HepG2-hNTCP-C4 cells (Fig. 1C–G). The corresponding signals were significantly reduced in the cells treated with an HBV entry inhibitor, Myrcludex-B, but not in the cells treated with DMSO (Fig. 1C–G). These data suggested that HepG2-hNTCP-C4 cells are HBV-susceptible, in contrast to the parental HepG2 cells. The HepG2-hNTCP-C4 cell line also was susceptible to infection with HBV genotype C, which was derived from the serum of an HBV-infected patient (Fig. 1H and I).

3.2. HBV susceptibility of HepG2-hNTCP-C4 cells was augmented by pretreatment with DMSO

It has been reported that a prolonged HBV infection in primary human hepatocytes can be enhanced by pretreatment with DMSO [19]. Therefore, we examined whether pretreatment with DMSO affected HBV infection of HepG2-NTCP-C4 cells. The cells were pretreated with 3% DMSO for 24 h and then the HBV infectivity was investigated following the protocol as in Fig. 1. Immunofluorescence analysis revealed that approximately 50% of the DMSO-pretreated cells were HBc-positive at 12 days post-infection (Fig. 2A, middle), while only 10–20% of cells were HBc-positive cells in the absence of pretreatment (Fig. 1G, upper right). The effect of DMSO pretreatment on HBV susceptibility was both concentration-(Fig. 2B) and time-dependent (Fig. 2C).

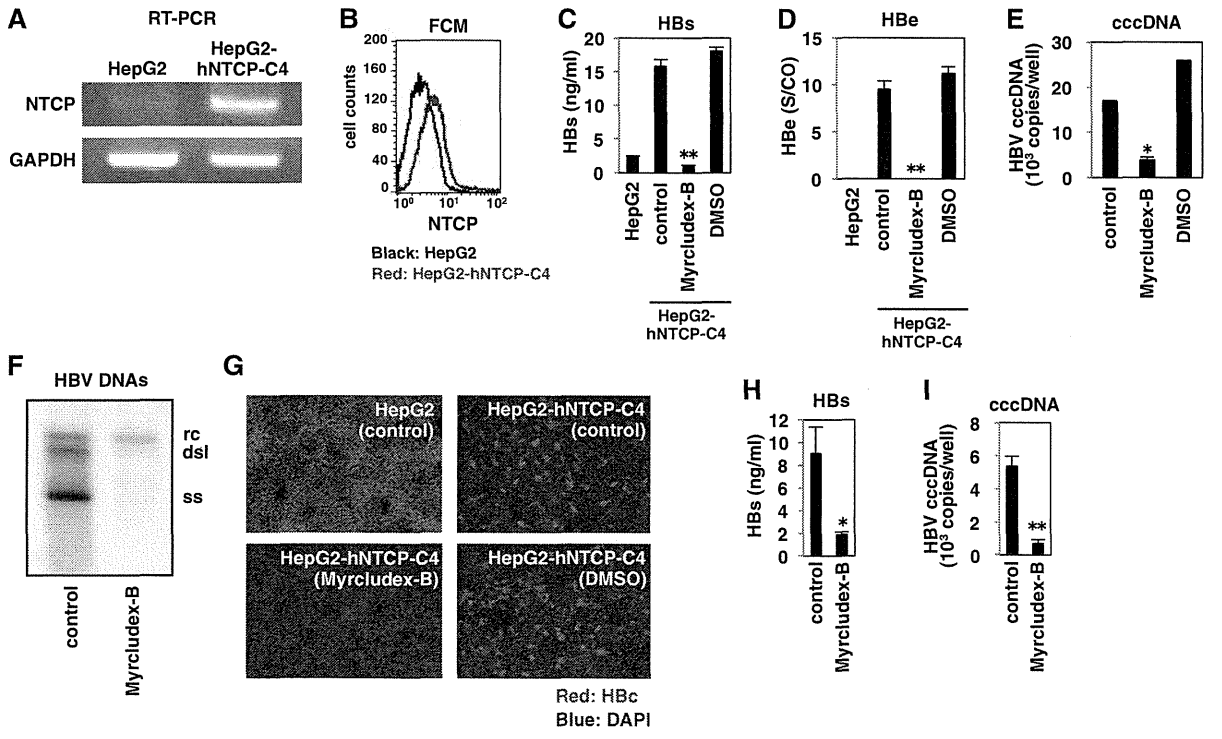

Fig. 1. Establishment of a cell line susceptible to hepatitis B virus (HBV) infection. (A) mRNAs for sodium taurocholate cotransporting polypeptide (NTCP) and GAPDH in HepG2 and HepG2-hNTCP-C4 cells were detected by RT-PCR. (B) NTCP protein on cell surface of HepG2 (black) and HepG2-hNTCP-C4 cells (red) was detected by flow cytometry. (C-G) HepG2-hNTCP-C4 or the parental HepG2 cells pretreated with or without 1 μM Myrcludex-B or vehicle (DMSO) for 3 h were inoculated with HBV (genotype D) for 16 h. After washing out of the free virus and the compounds, the cells were cultured for an additional 12 days in normal growth medium and then assayed for secretion of HBs (C) and HBe antigens (D) secreted in the culture supernatant, and for the presence of HBV covalently closed circular (ccc)DNA (E), HBV DNAs (F), and HBV core (HBc) proteins (G) in the cells. rc, dsl, and ss in (F) indicate relaxed circular, double strand linear, and single strand HBV DNA, respectively. Red and blue signals in (G) indicate HBc protein and nuclear staining, respectively. (H and I) Infection of blood-borne HBV into HepG2-hNTCP-C4 cells. HBV (genotype C) derived from an HBV-infected patient was used as an inoculum for the infection assay. Levels for HBs antigen in the culture supernatant (H) and HBV cccDNA in the cells (I) are shown. The data in C–E, H, and I show the means of three independent experiments. $^{*}P < 0.05$, $^{**}P < 0.01$.

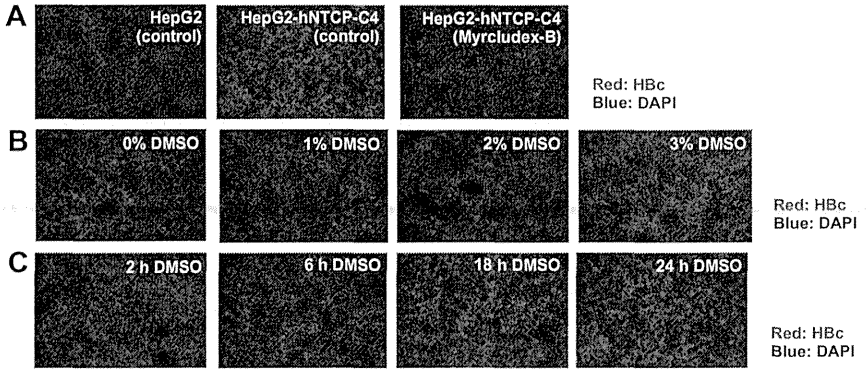

Fig. 2. HBV infection was facilitated by pretreatment of HepG2-hNTCP-C4 cells with DMSO. (A) HepG2 or HepG2-hNTCP-C4 cells preincubated with 3% DMSO for 24 h were inoculated with HBV in the presence of 3% DMSO for 16 h. Treatment with Myrcludex-B was used as a negative control for infection. At 12 days postinfection, HBc protein (red) and the nucleus (blue) were detected by immunofluorescence analysis. (B) Cells were pretreated by exposure for 24 h to various concentrations of DMSO (0–3%). (C) Cells were pretreated by exposure to 3% DMSO for various treatment times (2, 6, 18, and 24 h). HBc protein (red) and the nucleus (blue) were detected as in (A).

3.3. HBV infection was mediated by NTCP in HepG2-hNTCP-C4 cells

We used knockdown analysis to determine whether HBV infection of HepG2-hNTCP-C4 cells was mediated by NTCP. Transfection with siRNA against NTCP (si-NTCP) and GAPDH (si-GAPDH) specifically knocked down mRNA for NTCP and GAPDH, respectively, in HepG2-hNTCP-C4 cells (Fig. 3A). Consistent with the effect on transcript level, treatment with si-NTCP depleted NTCP protein on the cell surface (Fig. 3B). The HBV infection assay, performed as in Fig. 1, indicated that depletion of NTCP reduced the levels for HBs (Fig. 3C) and HBe antigens (Fig. 3D) in culture supernatant as well as HBV cccDNA (Fig. 3E) and HBc protein (Fig. 3F) in the cells at 12 days postinfection with HBV. These data suggested that HBV infection into HepG2-hNTCP-C4 cells was mediated by NTCP.

3.4. Evaluation of HBV entry inhibitors in HepG2-hNTCP-C4 cells

To determine whether HepG2-hNTCP-C4 cells could be used to evaluate anti-HBV activity of compounds, we examined the effect of known entry inhibitors in these cells. The cells were pretreated with compounds for 3 h and then inoculated with HBV for 16 h in the presence of compounds (Fig. 4A). Inoculation with HBV was followed by culturing of the cells in normal growth medium for an additional 12 days until detection of HBs antigen in the culture supernatant and cccDNA in the cells (Fig. 4A). This protocol has been used previously to evaluate the entry inhibition activity of compounds [20]. Treatment with anti-HBs neutralizing Ab, but not that with a non-relevant anti-FLAG Ab, inhibited HBV infection (Fig. 4B). Heparin and dextran sulfate, which have been reported to inhibit HBV attachment to the target cells [21], also reduced HBV infection (Fig. 4C). In addition, known NTCP substrates and inhibitors, including ursodeoxycholate, cholate, progesterone, and bromosulfophthalein [12], blocked HBV infection in this assay (Fig. 4D). We recently identified that cyclosporin A (CsA) and its analogs blocked HBV entry through inhibition of interaction between NTCP and the HBV large surface protein [20]. As shown in Fig. 4E, CsA and its analogs inhibited HBV infection in the present assay, with CsB showing the highest potency for inhibition of HBV infection among Cs analogs (Fig. 4E). These data indicate that HepG2-hNTCP-C4 cells are useful for evaluating the effect of HBV entry inhibitors.

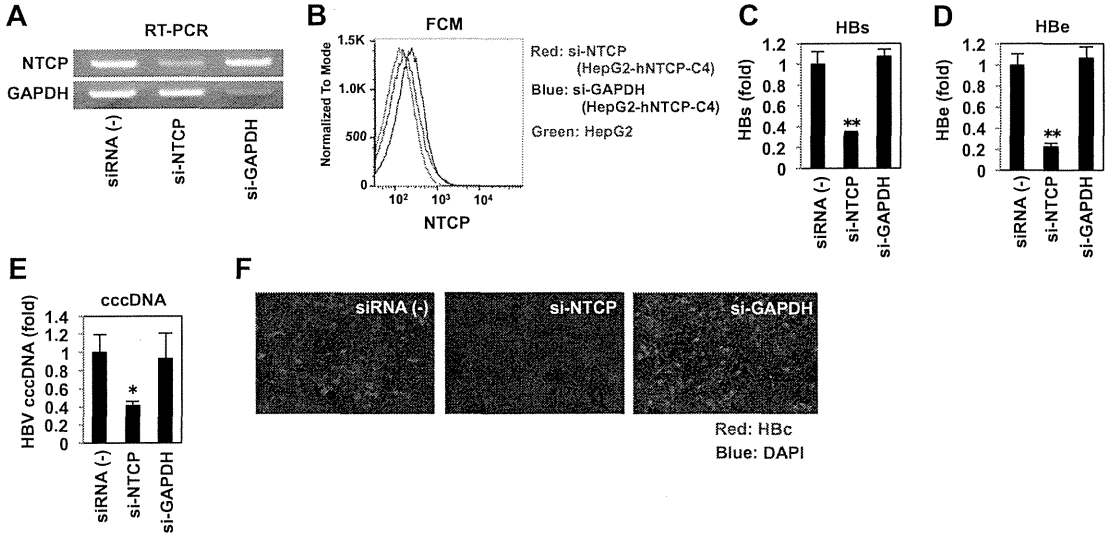

Fig. 3. HBV infection of HepG2-hNTCP-C4 cells was mediated by NTCP. (A) HepG2-hNTCP-C4 cells were transfected (for 48 h) with or without [siRNA(−)] siRNAs against NTCP (si-NTCP) or GAPDH (si-GAPDH), and mRNA expression levels of NTCP and GAPDH were detected by RT-PCR. (B) Parental HepG2 and HepG2-hNTCP-C4 cells were transfected (for 48 h) with or without si-NTCP or si-GAPDH, and cell surface-displayed NTCP protein was detected by flow cytometry. The red, blue, and green lines indicate the signal in HepG2-hNTCP-C4 cells treated with si-NTCP, HepG2-hNTCP-C4 cells treated with si-GAPDH, and HepG2 cells, respectively. (C–F) The cells prepared as in (A) were infected with HBV according to the protocol shown in Fig. 1. Culture supernatants were assayed for levels of secreted HBs (C) and HBe (D) antigens, and cells were assayed for intracellular levels of HBV cccDNA (E) and HBc protein (F). The red and blue signals in (F) indicate HBc and nuclear staining, respectively.

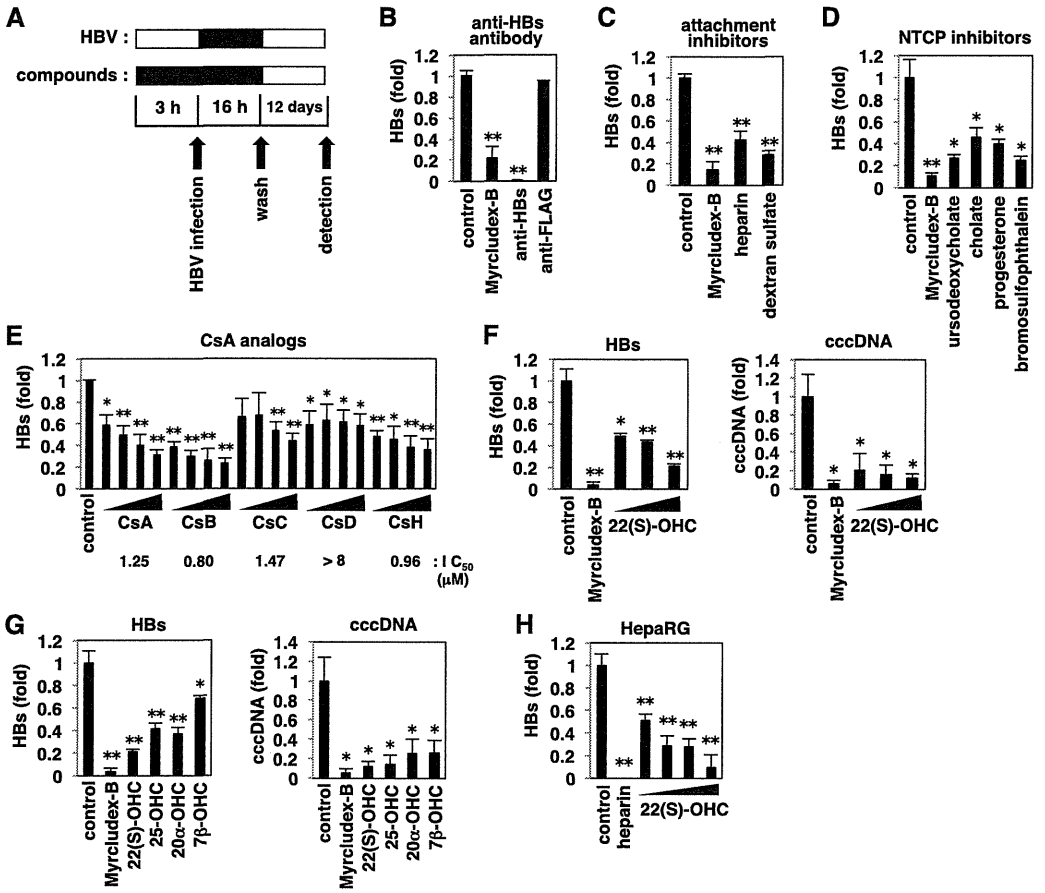

Fig. 4. Evaluation of HBV entry inhibitors in HepG2-hNTCP-C4 cells. (A) Schematic representation of the experimental procedure for evaluating HBV entry inhibition. HepG2-hNTCP-C4 cells were pretreated with or without compounds for 3 h and then inoculated with HBV for 16 h. After washing out of free HBV and the compounds, the cells were cultured with normal culture medium in the absence of compounds for an additional 12 days, and HBs antigen in the culture supernatant and/or HBV cccDNA in the cells were detected. Black and white bars show period of treatment and without treatment, respectively. (B–G) HepG2-hNTCP-C4 cells were treated with or without 1 μM Myrcludex-B, 10 μg/ml anti-HBs or anti-FLAG Ab (B); HBV attachment inhibitors including 100 IU/ml heparin and 1 mg/ml dextran sulfate (C); NTCP inhibitors including 100 μM ursodeoxycholate, 100 μM cholate, 40 μM progesterone, and 100 μM bromosulfophthalein (D); cyclosporins (CsA, CsB, CsC, CsD, CsH) at 1, 2, 4, and 8 μM (E); 22(S)-hydroxycholesterol (OHC) at 11, 33, and 100 μM (F); or oxysterols including 22(S)-OHC, 25-OHC, 20α-OHC, and 7β-OHC at 100 μM (G). For each assay, the cells were infected with HBV as shown in (A) and the levels of HBs antigen secreted into the culture supernatant and/or cccDNA in the cells were detected. Pretreatment time of compounds in (F) and (G) was 6 h, instead of 3 h. IC_{50}s of cyclosporin derivatives calculated in this assay are shown below the graph in (E). (H) HepaRG cells were treated with or without various concentrations of 22(S)-OHC (0.3, 0.9, 3, and 9 μM) and infected with HBV according to the protocol shown in (A). HBV infection was monitored by detecting the level of HBs secreted into the culture supernatant.

As there are only reverse transcriptase inhibitors currently available as anti-HBV drugs that inhibit the HBV life cycle, development of new anti-HBV agents targeting different steps in the HBV life cycle are greatly needed [1–4]. We therefore screened for compounds that blocked HBV entry by following the same protocol as in Fig. 4A. We found that an oxysterol, 22(S)-hydroxycholesterol (OHC), reduced HBV infection in a dose-dependent manner (Fig. 4F). Other oxysterols, 25-OHC, 20α-OHC, and 7β-OHC, also significantly decreased HBV infection (Fig. 4G). To validate this result, we repeated the assay using HepaRG cells, a line that frequently has been used in HBV entry experiments [14]. We found that 22(S)-OHC also reduced HBV infection of HepaRG cells in a dose-dependent manner (Fig. 4H), suggesting that the observed inhibitory effect of oxysterols reflects a genuine inhibition of HBV infection.

Thus, we have newly established a cell line that is susceptible to HBV infection. HepG2-hNTCP-C4 cells exhibited approximately 50% of HBV-infection positive cells (Fig. 2A), while maximum HBV infection of HepaRG cells was reported to be only 7% [16] or 20% [22] of the total population. These cells are expected to be useful for analyzing the molecular mechanisms of HBV infection, given that HepG2-derived cells show higher efficiency of transfection with expression plasmids and siRNAs than the current available HBV-susceptible PHH, PTH, and HepaRG cells. HepG2-hNTCP-C4 cells will facilitate knockdown analysis of host factors to define their roles in infection and screenings of compounds to identify novel inhibitors of HBV infection. As an example, we demonstrated here that oxysterols blocked HBV infection. The molecular mechanisms whereby oxysterols inhibit HBV infection are now under investigation. These analyses will be important for understanding the mechanisms of HBV infection as well as for developing new anti-HBV agents.

Acknowledgments

HepAD38 cells were kindly provided by Dr. Christoph Seeger at Fox Chase Cancer Center. Myrcludex-B, a pre-S1 lipopeptide, was kindly provided by Dr. Stephan Urban at University Hospital Heidelberg. We also are grateful to all of the members of Department of Virology II, National Institute of Infectious Diseases. This study was supported by Grants-in-aid from the Ministry of Health, Labor, and Welfare, Japan, from the Ministry of Education, Culture, Sports, Science, and Technology, Japan, and from Japan Society for the Promotion of Science, and from the Research on Health Sciences Focusing on Drug Innovation from the Japan Health Sciences Foundation.

References

[1] D. Grimm, R. Thimme, H.E. Blum, HBV life cycle and novel drug targets, Hepatol. Int. 5 (2011) 644–653.

[2] J.M. Pawlotsky, G. Dusheiko, A. Hatzakis, D. Lau, G. Lau, T.J. Liang, S. Locarnini, P. Martin, D.D. Richman, F. Zoulim, Virologic monitoring of hepatitis B virus therapy in clinical trials and practice: recommendations for a standardized approach, Gastroenterology 134 (2008) 405–415.

[3] M. Rapicetta, C. Ferrari, M. Levrero, Viral determinants and host immune responses in the pathogenesis of HBV infection, J. Med. Virol. 67 (2002) 454–457.

[4] F. Zoulim, Hepatitis B virus resistance to antiviral drugs: where are we going?, Liver Int 31 (Suppl. 1) (2011) 111–116.

[5] P. Gripon, S. Rumin, S. Urban, J. Le Seyec, D. Glaise, I. Cannie, C. Guyomard, J. Lucas, C. Trepo, C. Guguen-Guillouzo, Infection of a human hepatoma cell line by hepatitis B virus, Proc. Natl. Acad. Sci. USA 99 (2002) 15655–15660.

[6] D. Glebe, S. Urban, Viral and cellular determinants involved in hepadnaviral entry, World J. Gastroenterol. 13 (2007) 22–38.

[7] J.M. Gottwein, J. Bukh, Cutting the gordian knot-development and biological relevance of hepatitis C virus cell culture systems, Adv. Virus Res. 71 (2008) 51–133.

[8] H. Yan, G. Zhong, G. Xu, W. He, Z. Jing, Z. Gao, Y. Huang, Y. Qi, B. Peng, H. Wang, L. Fu, M. Song, P. Chen, W. Gao, B. Ren, Y. Sun, T. Cai, X. Feng, J. Sui, W. Li, Sodium taurocholate cotransporting polypeptide is a functional receptor for human hepatitis B and D virus, Elife 1 (2012) e00049.

[9] M.S. Anwer, B. Stieger, Sodium-dependent bile salt transporters of the SLC10A transporter family: more than solute transporters, Pflugers Arch. (2013) (Epub ahead of print).

[10] P.J. Meier, B. Stieger, Bile salt transporters, Annu. Rev. Physiol. 64 (2002) 635–661.

[11] C. Seeger, W.S. Mason, Sodium-dependent taurocholic cotransporting polypeptide: a candidate receptor for human hepatitis B virus, Gut 62 (2013) 1093–1095.

[12] R.B. Kim, B. Leake, M. Cvetkovic, M.M. Roden, J. Nadeau, A. Walubo, G.R. Wilkinson, Modulation by drugs of human hepatic sodium-dependent bile acid transporter (sodium taurocholate cotransporting polypeptide) activity, J. Pharmacol. Exp. Ther. 291 (1999) 1204–1209.

[13] S.K. Ladner, M.J. Otto, C.S. Barker, K. Zaifert, G.H. Wang, J.T. Guo, C. Seeger, R.W. King, Inducible expression of human hepatitis B virus (HBV) in stably transfected hepatoblastoma cells: a novel system for screening potential inhibitors of HBV replication, Antimicrob. Agents Chemother. 41 (1997) 1715–1720.

[14] K. Watashi, G. Liang, M. Iwamoto, H. Marusawa, N. Uchida, T. Daito, K. Kitamura, M. Muramatsu, H. Ohashi, T. Kiyohara, R. Suzuki, J. Li, S. Tong, Y. Tanaka, K. Murata, H. Aizaki, T. Wakita, Interleukin-1 and tumor necrosis factor-alpha trigger restriction of hepatitis B virus infection via a cytidine deaminase activation-induced cytidine deaminase (AID), J. Biol. Chem. 288 (2013) 31715–31727.

[15] S. Mita, H. Suzuki, H. Akita, H. Hayashi, R. Onuki, A.F. Hofmann, Y. Sugiyama, Inhibition of bile acid transport across Na+/taurocholate cotransporting polypeptide (SLC10A1) and bile salt export pump (ABCB 11)-coexpressing LLC-PK1 cells by cholestasis-inducing drugs, Drug Metab. Dispos. 34 (2006) 1575–1581.

[16] A. Schulze, K. Mills, T.S. Weiss, S. Urban, Hepatocyte polarization is essential for the productive entry of the hepatitis B virus, Hepatology 55 (2012) 373–383.

[17] M. Koyanagi, M. Hijikata, K. Watashi, O. Masui, K. Shimotohno, Centrosomal P4.1-associated protein is a new member of transcriptional coactivators for nuclear factor-kappaB, J. Biol. Chem. 280 (2005) 12430–12437.

[18] P. Gripon, I. Cannie, S. Urban, Efficient inhibition of hepatitis B virus infection by acylated peptides derived from the large viral surface protein, J. Virol. 79 (2005) 1613–1622.

[19] P. Gripon, C. Diot, A. Corlu, C. Guguen-Guillouzo, Regulation by dimethylsulfoxide, insulin, and corticosteroids of hepatitis B virus replication in a transfected human hepatoma cell line, J. Med. Virol. 28 (1989) 193–199.

[20] K. Watashi, A. Sluder, T. Daito, S. Matsunaga, A. Ryo, S. Nagamori, M. Iwamoto, S. Nakajima, S. Tsukuda, K. Borroto-Esoda, M. Sugiyama, Y. Tanaka, Y. Kanai, H. Kusuhara, M. Mizokami, T. Wakita, Cyclosporin A and its analogs inhibit hepatitis B virus entry into cultured hepatocytes through targeting a membrane transporter NTCP, Hepatology, in press.

[21] A. Schulze, P. Gripon, S. Urban, Hepatitis B virus infection initiates with a large surface protein-dependent binding to heparan sulfate proteoglycans, Hepatology 46 (2007) 1759–1768.

[22] O. Hantz, R. Parent, D. Durantel, P. Gripon, C. Guguen-Guillouzo, F. Zoulim, Persistence of the hepatitis B virus covalently closed circular DNA in HepaRG human hepatocyte-like cells, J. Gen. Virol. 90 (2009) 127–135.

ISSN: 2157-7439

Journal of Nanomedicine & Nanotechnology

The International Open Access Journal of Nanomedicine & Nanotechnology

Special Issue Title:

Nanotechnology: Challenges & Perspectives in Medicine

Handling Editors

Malavosklish Bikram
University of Houston, USA

Available online at: OMICS Publishing Group (www.omicsonline.org)

Digital Object Identi er: http://dx.doi.org/10.4172/2157-7439.S5-010

Nanomedicine & Nanotechnology

Gilmore et al., J Nanomed Nanotechol 2014, S5
http://dx.doi.org/10.4172/2157-7439.S5-010

Research Article Open Access

Nanoimaging of ssRNA: Genome Architecture of the Hepatitis C Virus Revealed by Atomic Force Microscopy

Jamie L Gilmore[1], Hideki Aizaki[2], Aiko Yoshida[1], Katashi Deguchi[1], Masahiro Kumeta[1], Julia Junghof[1], Takaji Wakita[2] and Kunio Takeyasu[1]*

[1]*Laboratory of Plasma Membrane and Nuclear Signaling, Kyoto University Graduate School of Biostudies, Yoshida-Konoe, Sakyo-ku, Kyoto 606-8501, Japan*
[2]*Virus Division II, National Institute of Infectious Diseases, Toyama, Shinjuku-ku, Tokyo 162-8640, Japan*

Abstract

The complex structures that RNA molecules fold into play important roles in their ability to perform various functions in the cell. The structure and composition of viral RNA influences the ability of the virus to implement the various stages of the viral lifecycle and can influence the severity of the virus effects on the host. Although many individual secondary structures and some tertiary interactions of the Hepatitis C virus genome have previously been identified, the global 3D architecture of the full 9.6 kb genome still remains uncertain. One promising technique for the determination of the overall 3D structure of large RNA molecules is nanoimaging with Atomic Force Microscopy. In order to get an idea of the structure of the HCV genome, we imaged the RNA prepared in the presence of Mg^{2+}, which allowed us to observe the compact folded tertiary structure of the viral genome. In addition, to identify individual structural elements of the genome, we imaged the RNA prepared in the absence of Mg^{2+}, which allowed us to visualize the unfolded secondary structure of the genome. We were able to identify a recurring single stranded region of the genome in many of the RNA molecules which was about 58 nm long. This method opens up a whole new avenue for the study of the secondary and tertiary structure of long RNA molecules. This ability to ascertain RNA structure can aid in drawing associations between the structure and the function of the RNA in cells which is vital to the development of potential antiviral therapies.

Keywords: Hepatitis C Virus; Atomic Force Microscopy; Untranslated region

Abbreviations: HCV: Hepatitis C Virus; AFM: Atomic Force Microscopy; UTR: Untranslated Region

Introduction

HCV is a worldwide epidemic, with about 150 million people worldwide infected and 350,000 deaths per year [1]. There is no vaccine for hepatitis C and treatments have met with limited success [2]. Given how pervasive HCV is, a better understanding of the virus may lead to important new discoveries which can help to highlight new avenues by which to treat individuals infected with the virus. Since HCV was originally cloned in 1989 [3], numerous studies have tried to understand the structure of the viral RNA, mainly in the conserved untranslated regions (UTRs) of the genome. Structural motifs that have been identified include the internal ribosome entry site (IRES) located in the 5'-UTR [4-17], the poly-U/UC region and 3'X RNA regions located in the 3'-UTR [18-24], and some stem loops in the coding region [25-29]. Additionally many long-range contacts between various regions of the genome have been reported [21,30-35]. Despite the vast number of reports on various structural features of the HCV genome, the full 3D architecture of the full genome remains uncertain.

Most techniques generally study bits and pieces of a single stranded (ss)RNA genome and hope to eventually arrive at the final global genome structure over time, or they provide data about various interactions within the molecule without providing 3D information [36]. The ability of Atomic Force Microscopy (AFM) to directly visualize the nanostructure of the whole genome in a variety of configurations in a single experiment makes it a very useful technique to assess the folded structures formed by a variety of ssRNA molecules. The usefulness of AFM for evaluating the nanometer scale architecture of biological molecules [37] was realized soon after the inception of the technology [38]. AFM has been used extensively for imaging of DNA with applications ranging from the study of DNA dynamics [39], DNA-protein interactions [40-45], to DNA origami structures [46,47]. However, techniques for obtaining reproducible ssRNA images have been slower to develop, leading to far fewer AFM imaging studies on ssRNA, although the nanometer scale resolution of AFM makes it a valuable tool for revealing the organization of ssRNA structures. Most AFM studies which have visualized ssRNA have used Mg^{2+} concentration of 4-10 mM [48-52]. However, a couple of early studies [53,54], as well as a couple others studies of viral RNA [55,56] have achieved more extended ssRNA configurations using low salt solutions. It is well documented that ions play a much larger role in the folding of RNA tertiary structures, but play a minimal role in the formation of secondary structures formed by Watson-Crick base pairing of the nucleotides in the RNA chain [57-59]. Thus, by imaging various ssRNA molecules prepared without the addition of Mg^{2+} ions, we should be able to get valuable information about the individual secondary structural motifs in the genome and and connectivity of the molecule.

In this study, we developed a method to observe both the secondary and tertiary structure of the full 9678 nt HCV genome with nanometer resolution using AFM. By omitting Mg^{2+} from the buffer used to dilute the RNA prior to AFM imaging, we were able to observe the secondary structure of the molecule. The molecules had a linear configuration with various appendages extending from the molecule. Some commonly

***Corresponding author:** Kunio Takeyasu, Laboratory of Plasma Membrane and Nuclear Signaling, Kyoto University Graduate School of Biostudies, Sakyo-ku Yoshida-Konoe, Kyoto 606-8501, Japan, Tel/Fax: +81-75-753-6852; E-mail: takeyasu@lif.kyoto-u.ac.jp

Received January 27, 2014; **Accepted** February 22, 2014; **Published** February 24, 2014

Citation: Gilmore JL, Aizaki H, Yoshida A, Deguchi K, Kumeta M, et al. (2014) Nanoimaging of ssRNA: Genome Architecture of the Hepatitis C Virus Revealed by Atomic Force Microscopy. J Nanomed Nanotechol S5: 010. doi:10.4172/2157-7439.S5-010

observed structural features were present in these molecules, including one end with a 58 nm long single stranded region and another end with a sharp kink followed by a region with a beaded appearance lacking appendages. The single stranded region observed is likely to be the poly-U/UC motif which is conserved across HCV genomes [18-24]. The morphology of homopolymeric ssRNA was further verified by imaging an ssRNA transcript of the importin-β coding region prepared *in vitro* with and without a poly(A) tail.

Materials and Methods

RNA

The JFH-1 genomic RNA (accession no. AB047639) is a 9678 nt positive strand RNA [60]. The JFH-1 strain, belonging to genotype 2a, is the first strain of the Hepatitis C virus isolated from a patient which could be successfully replicated in cell culture [61]. The JFH-1 RNA used for these experiments was synthesized *in vitro* by T7 polymerase transcription and purified with the Zymoclean kit [62,63]. The polyadenylated importin-β mRNA was prepared *in vitro*. Mouse cDNA for importin-β was cloned into the pTD vector (Shimadzu Corp., Japan) and transcribed with the MEGAscript T7 kit (Ambion, USA). The RNA was polyadenylated with the Poly(A) Tailing kit (Ambion, USA) and purified by LiCl precipitation.

AFM sample preparation

All pieces of mica were cut with a hole punch and super-glued to a 15 mm metal specimen disc at least a day prior to sample deposition for AFM. The JFH-1 HCV RNA was prepared by diluting the RNA sample to 0.1-0.5 ng/μL in buffer EB (10 mM Tris, pH 8.5) from Qiagen or in a buffer containing 20 mM Tris, 1.5 mM $MgCl_2$, and 1.5 mM dithiothreitol (DTT). The sample was then heated to 65°C for 2 mins, and then kept at room temperature until deposition. Just prior to sample deposition, a piece of mica affixed to a 15 mm metal specimen disc was freshly cleaved and 10 μL 10 mM spermidine was deposited on the mica and incubated for 3.5 mins. The spermidine was then washed away by washing three times with 1 mL of milli-Q water immediately followed by deposition of 10 μL of the RNA sample for 3.5 mins. The sample was then washed again three times with 1 mL of milli-Q water and dried with a stream of nitrogen. The sample was immediately used for AFM imaging.

AFM imaging and analysis

AFM imaging was performed with the Multimode AFM with a Nanoscope III or IV controller and with an E or a J scanner (Digital instruments, Inc., USA). The microscope was operated in the Tapping Mode™ at a scanning rate of 0.5-1.0 Hz. Rectangular silicon cantilevers with sharpened tetrahedral tips were used (OMCL AC160TS, Olympus Corp., Japan). These probes had a tip radius of about 7 nm, a resonant frequency of about 300 kHz, and a spring constant of about 26 N/m. Images displayed in this publication were flattened in the Nanoscope (v.5.31 r1) software and exported as jpegs. Images were analyzed with the Gwyddion software (Department of Metrology, Czech Metrology Institute, Czech Republic). The raw SPM images were opened in the Gwyddion software and processed by correcting the horizontal scars, correcting lines by matching the height median, leveling the data to make facets point upwards, leveling the data by mean plane subtraction, and removing the polynomial background (3rd degree). The RNA molecules were marked by selecting all molecules above a 0.15-0.20 nm threshold and then removing all grains smaller then 60-70 px^2. The edit mask tool in the subtract selection mode was used to deselect molecules from the periphery of the image. The distributions of various grain characteristics were then exported as a raw data file and then the measure individual grain tool was used to click on each molecule and record the zero basis volume and minimum circumcircle radius of each one. The values were inserted into the Origin Lab software (OriginLab Corp., USA), plotted into histograms, and fitted with Gaussian curves to obtain the center value(s) for each histogram. The errors reflect the standard deviation of the Gaussian distribution. The contour length of the molecules was measured and height profiles were generated with the Femtoscan software (Advanced Technologies Center, Moscow, Russia). The scatterplot was plotted and fitted with a linear regression curve with the y-intercept set to 0 in Microsoft Office Excel.

Results and Discussion

AFM imaging of HCV RNA tertiary structure

In our experiments, we used the full positive-stranded ssRNA HCV genome which is 9678 nt in length. When the RNA was heated for 2 mins, at 65°C in buffer containing 1.5 mM $MgCl_2$ just prior to deposition on the mica surface for imaging, the RNA molecules had a compact morphology with a variety of appendages extending from the structures (Figure 1A and 1B). A histogram of the volume distribution of these molecules was fitted with a single peak at 3823 ± 1857 nm^3 (Figure 1C). The diameter of the smallest enclosing circle for this Mg^{2+}-containing buffer was 136 ± 40 nm (Figure 1D). The diameter of HCV viral particles has been reported to be about 30-75 nm [64-74], so the RNA is likely to be compacted 2-5 times more when it is packaged into the capsid.

AFM imaging of HCV RNA secondary structure

Since Mg^{2+} is required for many tertiary contacts to form, but not required for the formation of RNA secondary structures formed primarily by Watson-Crick base-pairing [57-59], we should be able to image the secondary structure without the formation of tertiary contacts by diluting the RNA in Mg^{2+}-free buffer. After heating for 2 mins at 65°C in this buffer just prior to deposition, the morphology of the RNA was markedly different (Figure 2A and 2B). These RNA molecules had a linearized morphology with various small appendages along the molecule. When the volume of these molecules was analyzed, there was a main peak at 4136 ± 1768 nm^3 (Figure 2C). This is close to the volume of the HCV genome molecules in the Mg^{2+} buffer (Figure 1C), suggesting that single molecules are observed in both set of conditions. There is also a larger peak in the volume histogram at 8691 ± 436 nm^3. This suggests that some of the molecules may actually have dimerized in these images. The diameter of the smallest enclosing circle was 219 ± 63 nm (Figure 2D), 1.6 times larger than the molecules in the Mg^{2+}-containing buffer.

Structural Analysis of HCV RNA

To get a better idea of the secondary structure of the HCV RNA molecules, additional dimensional analysis was performed. In Figure 3, two molecules which appeared to have some structural similarities are shown. These two molecules show a common structural characteristic of one end with a blob with a height of about 2 nm followed by a 35-76 nm long region of the molecule with heights of about 0.5 nm (Figure 3A, left, box outlines). This area likely represents an unpaired single stranded region of the HCV genome. The contour of the molecules extended for lengths of 582 nm (top) and 470 nm (bottom). Height profiles for each of these molecules showed 29 peaks (top) or 27 peaks (bottom) with 17 (top) or 16 (bottom) visibly protruding appendages

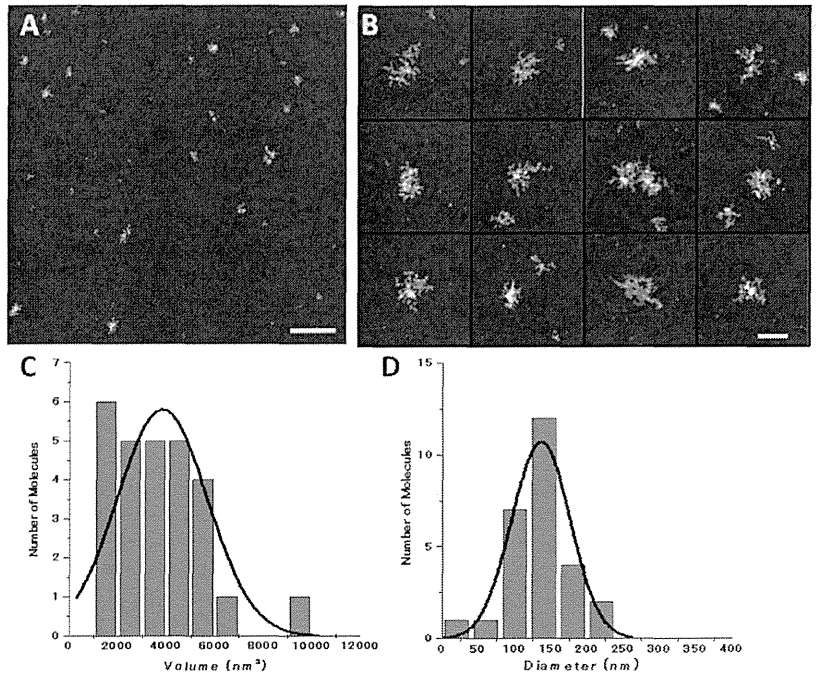

Figure 1: AFM imaging and analysis of HCV RNA deposited in Mg^{2+}-containing buffer. A representative 3×3 μm² image (**A** scale bar=0.4 μm) along with a gallery of 0.4×0.4 μm² images (**B** scale Bar=0.1 μm) for RNA deposited in buffer containing 1.5 mM Mg^{2+} cations. Histograms of the volume (**C**) and diameter of the smallest enclosing circle (**D**).

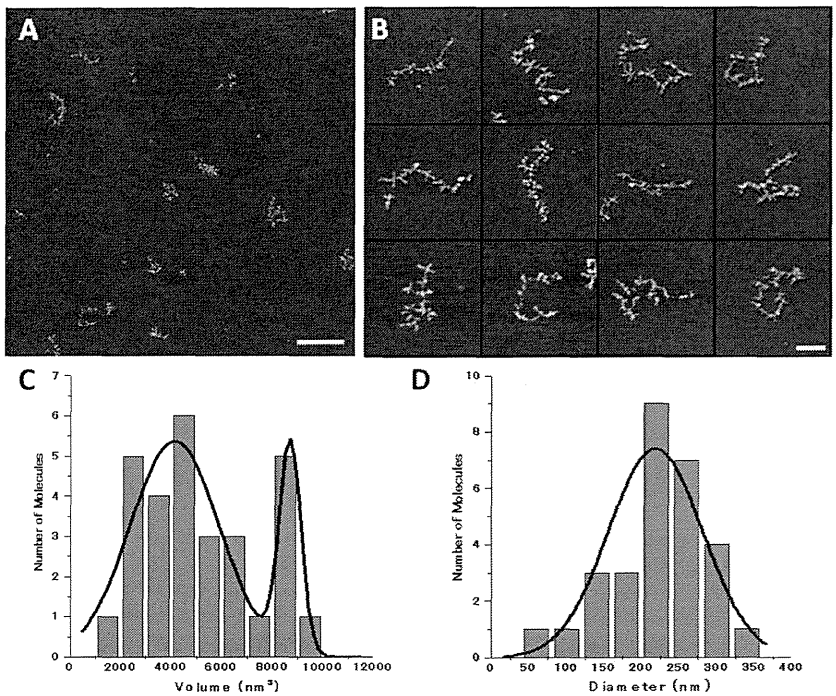

Figure 2: AFM imaging and analysis of HCV RNA deposited in Mg^{2+}-free buffer. A representative 3×3 μm² image (**A**, scale bar=0.4 μm) along with a gallery of 0.4×0.4 μm² images (**B**, scale Bar=0.1 μm) for RNA deposited in buffer lacking Mg^{2+} cations . Histograms of the volume (**C**) and diameter of the smallest enclosing circle (**D**).

(Figure 3A, graphs). These values can vary considerably depending on the orientation of the molecule on the mica surface. The other end of the molecules has an appendage-free region with a 'beaded' appearance showing variable structures with heights of about 2-3 nm preceded by a sharp kinked region (Figure 3A, left, arrows).

Additional molecules displaying this single-stranded morphology are displayed in Figure 3B. A histogram of the length of this single stranded region results in a single peak centered around the value of 58 ± 8 nm (Figure 3C). It is likely that this region corresponds to the poly-U/UC region present in this RNA molecule. The poly-U/C region is conserved throughout all HCV genotypes, but varies in length [18]. In the JFH-1 genome used in this study, this region is 103 nt long. Varying the length or composition of this region has been reported to effect the efficiency of viral replication [19-21] as well as to influence recognition of the genome by the RIG-I protein which is necessary for the host cell to mount an Interferon (IFN)-mediated immune response to the virus [22-24]. Assuming that this single stranded regions is actually 103 nt long (the whole poly-U/UC region is unpaired and the regions immediately flanking it are paired), it would mean that, according to our measured length (58 nm), the length per nucleotide of the single stranded region is 0.56 nm. In a previous force measurement study with homopolymeric ribonucleotides, molecules 1500-4000 nt in long were stretched to a length of about 1600 nm. This means that the length per nucleotide should be about 0.4-1.0 nm, in good agreement with our calculated value [75,76]. The small blob at the end of the single stranded region is likely the 98 nt 3' X-RNA which is a well studied region immediately flanking the poly-U/UC region and has been reported to form either two or three stem loops [35].

Verification of RNA homopolymer morphology and ssRNA volume

To further verify the morphology of homopolymeric single-stranded RNA with AFM, an 3890 nt importin-β ssRNA transcript was also imaged (Figure 4). This transcript is not a true mRNA because it lacks the 5' and 3'-UTRs. The importin-β ssRNA was prepared by *in vitro* transcription in two different ways. Initially, the ssRNA was simply transcribed from cDNA with T7 polymerase and directly imaged (Figure 4A). The same RNA was then treated with polyadenylate polymerase to add a random number of adenine residues to the molecules and imaged (Figure 4B). The addition of the poly(A) tail

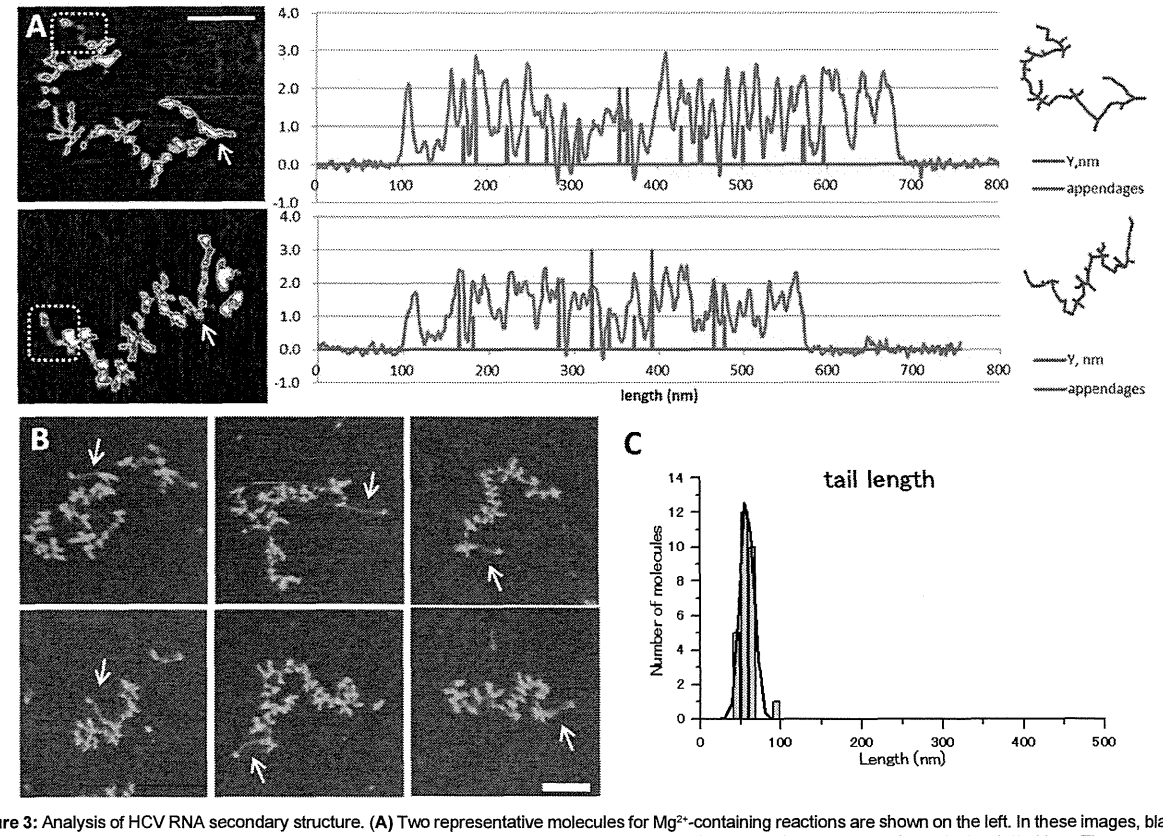

Figure 3: Analysis of HCV RNA secondary structure. **(A)** Two representative molecules for Mg^{2+}-containing reactions are shown on the left. In these images, black ~0 nm, blue ~0.5 nm, green ~1.0 nm, red ~1.5 nm, and white ~2 nm and higher. The single stranded region of the genome is shown in the dotted box. The arrows point to the kinked region of the genome preceding the appendage-free region of the genome. Bar=80 nm. To the right of each image, a contour plot profile corresponding to each molecule is displayed with the blue line corresponding to the height of features along the length backbone of the molecule and the red line corresponding to the number of appendages protruding out from the molecule along the backbone. Each plot starts at 100 nm along the background of the image. The molecule is then traced starting from the end outlined with the box in the images at the left. A trace of the molecule is shown to the right of each plot. **(B)** Six representative 0.4×0.4 μm^2 images of molecules exhibiting the single stranded 'tail' morphology → at the end of the molecule. Bar=100 nm **(C)** A histogram of the length of the tail region of the molecules which exhibited this morphology.

shows a single stranded morphology similar to what was observed for the end of the viral RNA molecules. Along the mainly single stranded region, there are often kinks, or 'knobs" and some apparent double-stranded regions. This observation is corroborated by previous AFM imaging which also observed a 'knob' like structures along poly(A) RNA molecules [54]. Additionally, the crystal structure of a poly(A) duplex has been resolved to 1 Å resolution [77].

Measurement of the contour length of the importin-β poly(A) tails showed a very broad distribution of values ranging from 40-830 nm long (Figure 4C). Attempting to fit the broad distribution with a Gaussian curve resulted in a value of 125 ± 88 nm, suggesting that the majority of the poly(A) tails were about twice as long as observed for the viral RNA and the standard deviation of the distribution is 11 times higher. Although the morphologies of the homopolymeric RNA molecules were similar, past studies have reported results suggesting that homopolymeric chains of different nucleotides do not behave exactly the same. For example, poly(G) forms tetrads [78]. Poly(C) and poly(A) have been reported to form single-stranded helical regions which are reflected by plateaus when the chains are stretched resulting from a helix-coil transistion. However, when poly(U) is stretched, there are no plateaus, suggesting that it does not form helical domains [76].

Verification that the viral ssRNA structures we observed represent the full viral genome comes from comparing the measured volumes in of various ssRNA molecules to their molecular weight. The graph in Figure 4D shows how the measured volumes of four different kinds of ssRNA molecules relates to their length in nucleotides. The four molecules analyzed include the HCV RNA (3823 ± 1857 nm^3), the importin-β ssRNA without the poly(A) tail (1930 ± 437 nm^3), the 28S ribosomal (r)RNA (2688 ± 655 nm^3), and the 18S rRNA (921 ± 527 nm^3). By fitting these points with a linear regression curve, the volume measured using our method increases by 0.4 nm^3 per nucleotide of RNA. Images of the 18S and 28S rRNA molecules are shown in Figure 4E for reference.

Perspective

The ability of AFM to visualize Mg^{2+}-dependent structural changes of RNA opens up an exciting range of possibilities for what AFM can reveal about RNA in the future. For example, the ability of AFM to image molecules in aqueous environments opens up the exciting possibility of visualizing the folding/unfolding transitions of RNA using high-speed AFM (HS-AFM) [41-45]. Additionally, further refinement of the structural models could be gained by imaging individual portions of the

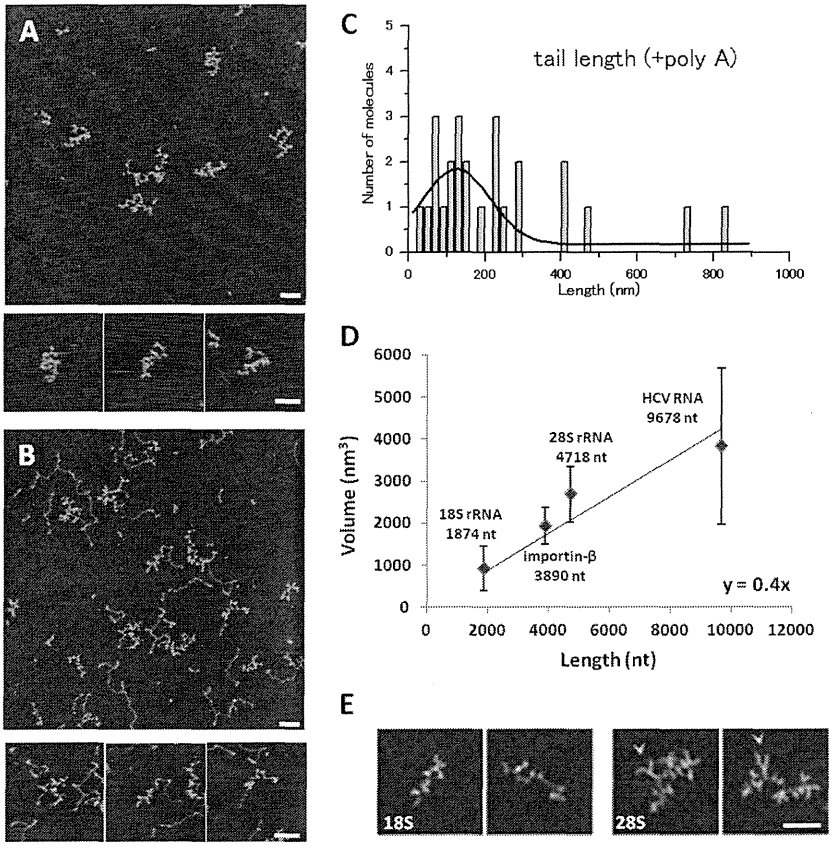

Figure 4: Imaging and analysis of importin-β ssRNA secondary structure. Representative 1.5×1.5 μm² images with a gallery of three 0.4×0.4 μm² images of importin-β mRNA without (**A**) and with (**B**) the poly A tail. (**C**) A histogram of the length of the poly(A) tail of the molecules in (**B**). (**D**) A graph demonstrating how the length of four different ssRNA molecules relates to the measured volume. Bars represent the standard deviation of the gaussian distribution. (**E**) Representative images of 18S and 28S rRNA molecules →All scale bars=100 nm.

RNA. Comparing these individual domains may aid in understanding how their structures relate to the structures observed in the full viral genome. Additionally, labeling strategies could be used to identify where a particular sequence may occur along an RNA backbone. In addition to labels, the interaction of various RNA-binding proteins with various RNA structures can also be studied. If a method to attach a RNA-binding protein or chemical to the AFM tip can be developed, recognition imaging [79-82] may also be used to assess which structural features of an RNA molecule the ligand interacts with. Also, proteins can be imaged along with the RNA to observe the effect they have on the viral structure. The ability of AFM to visualize global structural rearrangements of RNA may be a promising tool to investigate the role of RNA structures in viral processes for future studies, which could provide us with an understanding of how to control the spread of the virus in infected individuals.

Acknowledgements

R.W and K.T. are supported by a Grant-in-Aid for Scientific Research on Innovative Areas "Molecular basis of host cell competency in virus infection" (#24115003) from MEXT Japan. M.K. is supported by a Grant-in-Aid for Scientific Research on Innovative Areas "Spying minority in biological phenomena" (#24115512) from MEXT Japan.

References

1. World Health Organization (2013) Hepatitis C Fact Sheet no. 164. Geneva, Switzerland.
2. Zhu Y, Chen S (2013) Antiviral treatment of hepatitis C virus infection and factors affecting efficacy. World J Gastroenterol 19: 8963-8973.
3. Choo QL, Kuo G, Weiner a J, Overby LR, Bradley DW, et al. (1989) Isolation of a cDNA clone derived from a blood-borne non-A, non-B viral hepatitis genome. Science 244: 359-362.
4. Tsukiyama-Kohara K1, Iizuka N, Kohara M, Nomoto A (1992) Internal ribosome entry site within hepatitis C virus RNA. J Virol 66: 1476-1483.
5. Brown EA, Zhang H, Ping LH, Lemon SM (1992) Secondary structure of the 5' nontranslated regions of hepatitis C virus and pestivirus genomic RNAs. Nucleic Acids Res 20: 5041-5045.
6. Wang C, Le SY, Ali N, Siddiqui A (1995) An RNA pseudoknot is an essential structural element of the internal ribosome entry site located within the hepatitis C virus 5' noncoding region. RNA 1: 526-537.
7. Honda M, Ping LH, Rijnbrand RC, Amphlett E, Clarke B, et al. (1996) Structural requirements for initiation of translation by internal ribosome entry within genome-length hepatitis C virus RNA. Virology 222: 31-42.
8. Kieft JS, Zhou K, Jubin R, Murray MG, Lau JY, et al. (1999) The hepatitis C virus internal ribosome entry site adopts an ion-dependent tertiary fold. J Mol Biol 292: 513-529.
9. Lukavsky PJ, Otto GA, Lancaster AM, Sarnow P, Puglisi JD (2000) Structures of two RNA domains essential for hepatitis C virus internal ribosome entry site function. Nat Struct Biol 7: 1105-1110.
10. Kieft JS, Zhou K, Grech A, Jubin R, Doudna JA (2002) Crystal structure of an RNA tertiary domain essential to HCV IRES-mediated translation initiation. Nat Struct Biol 9: 370-374.
11. Kim I1, Lukavsky PJ, Puglisi JD (2002) NMR study of 100 kDa HCV IRES RNA using segmental isotope labeling. J Am Chem Soc 124: 9338-9339.
12. Lukavsky PJ1, Kim I, Otto GA, Puglisi JD (2003) Structure of HCV IRES domain II determined by NMR. Nat Struct Biol 10: 1033-1038.
13. Kieft JS (2008) Viral IRES RNA structures and ribosome interactions. Trends Biochem Sci 33: 274-283.
14. Rijnbrand R, Thiviyanathan V, Kaluarachchi K, Lemon SM, Gorenstein DG (2004) Mutational and structural analysis of stem-loop IIIC of the hepatitis C virus and GB virus B internal ribosome entry sites. J Mol Biol 343: 805-817.
15. Lukavsky PJ (2009) Structure and function of HCV IRES domains. Virus Res 139: 166-171.
16. Berry KE, Waghray S, Mortimer SA, Bai Y, Doudna JA (2011) Crystal structure of the HCV IRES central domain reveals strategy for start-codon positioning. Structure 19: 1456-1466.
17. Pérard J, Leyrat C, Baudin F, Drouet E, Jamin M (2013) Structure of the full-length HCV IRES in solution. Nat Commun 4: 1612.
18. Kolykhalov AA, Feinstone SM, Rice CM (1996) Identification of a highly conserved sequence element at the 3 ' terminus of hepatitis C virus genome RNA. These include?: Identification of a Highly Conserved Sequence Element at the 3? Terminus of Hepatitis C Virus Genome RNA. 70: 3363-3371.
19. Friebe P, Bartenschlager R (2002) Genetic analysis of sequences in the 3' nontranslated region of hepatitis C virus that are important for RNA replication. J Virol 76: 5326-5338.
20. Yi M, Lemon SM (2003) 3' nontranslated RNA signals required for replication of hepatitis C virus RNA. J Virol 77: 3557-3568.
21. You S, Rice CM (2008) 3' RNA elements in hepatitis C virus replication: kissing partners and long poly(U). J Virol 82: 184-195.
22. Saito T, Owen DM, Jiang F, Marcotrigiano J, Gale M Jr (2008) Innate immunity induced by composition-dependent RIG-I recognition of hepatitis C virus RNA. Nature 454: 523-527.
23. Uzri D, Gehrke L (2009) Nucleotide sequences and modifications that determine RIG-I/RNA binding and signaling activities. J Virol 83: 4174-4184.
24. Schnell G, Loo YM, Marcotrigiano J, Gale M Jr (2012) Uridine composition of the poly-U/UC tract of HCV RNA defines non-self recognition by RIG-I. PLoS Pathog 8: e1002839.
25. Tuplin A, Wood J, Evans DJ, Patel AH, Simmonds P (2002) Thermodynamic and phylogenetic prediction of RNA secondary structures in the coding region of hepatitis C virus. RNA 8: 824-841.
26. You S, Stump DD, Branch AD, Rice CM (2004) A cis-acting replication element in the sequence encoding the NS5B RNA-dependent RNA polymerase is required for hepatitis C virus RNA replication. J Virol 78: 1352-1366.
27. Lee H, Shin H, Wimmer E, Paul AV (2004) cis-acting RNA signals in the NS5B C-terminal coding sequence of the hepatitis C virus genome. J Virol 78: 10865-10877.
28. Tuplin a, Evans DJ, Simmonds P (2004) Detailed mapping of RNA secondary structures in core and NS5B-encoding region sequences of hepatitis C virus by RNase cleavage and novel bioinformatic prediction methods. J Gen Virol 85: 3037–3047.
29. Zhang J, Yamada O, Sakamoto T, Yoshida H, Araki H, et al. (2005) Inhibition of hepatitis C virus replication by pol III-directed overexpression of RNA decoys corresponding to stem-loop structures in the NS5B coding region. Virology 342: 276-285.
30. Friebe P, Boudet J, Simorre JP, Bartenschlager R (2005) Kissing-loop interaction in the 3' end of the hepatitis C virus genome essential for RNA replication. J Virol 79: 380-392.
31. Diviney S, Tuplin A, Struthers M, Armstrong V, Elliott RM, et al. (2008) A hepatitis C virus cis-acting replication element forms a long-range RNA-RNA interaction with upstream RNA sequences in NS5B. J Virol 82: 9008-9022.
32. Romero-López C, Berzal-Herranz A (2009) A long-range RNA-RNA interaction between the 5' and 3' ends of the HCV genome. RNA 15: 1740-1752.
33. Shetty S, Kim S, Shimakami T, Lemon SM, Mihailescu MR (2010) Hepatitis C virus genomic RNA dimerization is mediated via a kissing complex intermediate. RNA 16: 913-925.
34. Tuplin A, Struthers M, Simmonds P, Evans DJ (2012) A twist in the tail: SHAPE mapping of long-range interactions and structural rearrangements of RNA elements involved in HCV replication. Nucleic Acids Res 40: 6908-6921.
35. Shetty S, Stefanovic S, Mihailescu MR (2013) Hepatitis C virus RNA: molecular switches mediated by long-range RNA-RNA interactions? Nucleic Acids Res 41: 2526-2540.
36. Jaeger JA, SantaLucia J Jr, Tinoco I Jr (1993) Determination of RNA structure and thermodynamics. Annu Rev Biochem 62: 255-287.
37. Hansma PK, Elings VB, Marti O, Bracker CE (1988) Scanning tunneling microscopy and atomic force microscopy: application to biology and technology. Science 242: 209-216.
38. Binnig G, Quate CF, Gerber C (1986) Atomic force microscope. Phys Rev Lett 56: 930-933.
39. Suzuki Y, Yoshikawa Y, Yoshimura SH, Yoshikawa K, Takeyasu K (2011) Unraveling DNA dynamics using atomic force microscopy. Wiley Interdiscip Rev Nanomed Nanobiotechnol.

40. Shlyakhtenko LS, Gilmore J, Portillo A, Tamulaitis G, Siksnys V, et al. (2007) Direct visualization of the EcoRII-DNA triple synaptic complex by atomic force microscopy. Biochemistry 46: 11128-11136.

41. Crampton N, Yokokawa M, Dryden DT, Edwardson JM, Rao DN, et al. (2007) Fast-scan atomic force microscopy reveals that the type III restriction enzyme EcoP15I is capable of DNA translocation and looping. Proc Natl Acad Sci U S A 104: 12755-12760.

42. Gilmore JL, Suzuki Y, Tamulaitis G, Siksnys V, Takeyasu K, et al. (2009) Single-molecule dynamics of the DNA-EcoRII protein complexes revealed with high-speed atomic force microscopy. Biochemistry 48: 10492-10498.

43. Suzuki Y, Higuchi Y, Hizume K, Yokokawa M, Yoshimura SH, et al. (2010) Molecular dynamics of DNA and nucleosomes in solution studied by fast-scanning atomic force microscopy. Ultramicroscopy 110: 682-688.

44. Suzuki Y, Gilmore JL, Yoshimura SH, Henderson RM, Lyubchenko YL, et al. (2011) Visual analysis of concerted cleavage by type IIF restriction enzyme SfiI in subsecond time region. Biophys J 101: 2992-2998.

45. Sanchez H, Suzuki Y, Yokokawa M, Takeyasu K, Wyman C (2011) Protein-DNA interactions in high speed AFM: single molecule diffusion analysis of human RAD54. Integr Biol (Camb) 3: 1127-1134.

46. Suzuki Y, Endo M, Katsuda Y, Ou K, Hidaka K, et al. (2014) DNA origami based visualization system for studying site-specific recombination events. J Am Chem Soc 136: 211-218.

47. Suzuki Y, Endo M, Yang Y, Sugiyama H (2014) Dynamic assembly/disassembly processes of photoresponsive DNA origami nanostructures directly visualized on a lipid membrane surface. J Am Chem Soc 136: 1714-1717.

48. Noestheden M, Hu Q, Tonary AM, Tay LL, Pezacki JP (2007) Evaluation of chemical labeling strategies for monitoring HCV RNA using vibrational microscopy. Org Biomol Chem 5: 2380-2389.

49. Chernov KG, Curmi PA, Hamon L, Mechulam A, Ovchinnikov LP, et al. (2008) Atomic force microscopy reveals binding of mRNA to microtubules mediated by two major mRNP proteins YB-1 and PABP. FEBS Lett 582: 2875-2881.

50. Davis M, Sagan SM, Pezacki JP, Evans DJ, Simmonds P (2008) Bioinformatic and physical characterizations of genome-scale ordered RNA structure in mammalian RNA viruses. J Virol 82: 11824-11836.

51. Sagan SM, Nasheri N, Luebbert C, Pezacki JP (2010) The efficacy of siRNAs against hepatitis C virus is strongly influenced by structure and target site accessibility. Chem Biol 17: 515-527.

52. Wu B1, Grigull J, Ore MO, Morin S, White KA (2013) Global organization of a positive-strand RNA virus genome. PLoS Pathog 9: e1003363.

53. Hansma HG1, Revenko I, Kim K, Laney DE (1996) Atomic force microscopy of long and short double-stranded, single-stranded and triple-stranded nucleic acids. Nucleic Acids Res 24: 713-720.

54. Smith BL, Gallie DR, Le H, Hansma PK (1997) Visualization of poly(A)-binding protein complex formation with poly(A) RNA using atomic force microscopy. J Struct Biol 119: 109-117.

55. Kuznetsov YG, Daijogo S, Zhou J, Semler BL, McPherson A (2005) Atomic force microscopy analysis of icosahedral virus RNA. J Mol Biol 347: 41-52.

56. Archer EJ, Simpson MA, Watts NJ, O'Kane R, Wang B, et al. (2013) Long-range architecture in a viral RNA genome. Biochemistry 52: 3182-3190.

57. Brion P, Westhof E (1997) Hierarchy and dynamics of RNA folding. Annu Rev Biophys Biomol Struct 26: 113-137.

58. Tinoco I Jr, Bustamante C (1999) How RNA folds. J Mol Biol 293: 271-281.

59. Draper DE (2004) A guide to ions and RNA structure. RNA 10: 335-343.

60. Kato T, Furusaka A, Miyamoto M, Date T, Yasui K, et al. (2001) Sequence analysis of hepatitis C virus isolated from a fulminant hepatitis patient. J Med Virol 64: 334-339.

61. Kato T, Date T, Miyamoto M, Furusaka A, Tokushige K, et al. (2003) Efficient replication of the genotype 2a hepatitis C virus subgenomic replicon. Gastroenterology 125: 1808-1817.

62. Kato T, Date T, Murayama A, Morikawa K, Akazawa D, et al. (2006) Cell culture and infection system for hepatitis C virus. Nat Protoc 1: 2334-2339.

63. Wakita T (2009) Isolation of JFH-1 strain and development of an HCV infection system. Methods Mol Biol 510: 305-327.

64. He LF, Alling D, Popkin T, Shapiro M, Alter HJ, et al. (1987) Determining the size of non-A, non-B hepatitis virus by filtration. J Infect Dis 156: 636-640.

65. Yuasa T, Ishikawa G, Manabe S, Sekiguchi S, Takeuchi K, et al. (1991) The particle size of hepatitis C virus estimated by filtration through microporous regenerated cellulose fibre. J Gen Virol 72: 2021-2024.

66. Takahashi K, Kishimoto S, Yoshizawa H, Okamoto H, Yoshikawa A, et al. (1992) p26 protein and 33-nm particle associated with nucleocapsid of hepatitis C virus recovered from the circulation of infected hosts. Virology 191: 431-434.

67. Kaito M, Watanabe S, Tsukiyama-Kohara K, Yamaguchi K, Kobayashi Y, et al. (1994) Hepatitis C virus particle detected by immunoelectron microscopic study. J Gen Virol 75: 1755-1760.

68. Shimizu YK, Feinstone SM, Kohara M, Purcell RH, Yoshikura H (1996) Hepatitis C virus: detection of intracellular virus particles by electron microscopy. Hepatology 23: 205-209.

69. Wakita T, Pietschmann T, Kato T, Date T, Miyamoto M, et al. (2005) Production of infectious hepatitis C virus in tissue culture from a cloned viral genome. Nat Med 11: 791-796.

70. Gastaminza P, Kapadia SB, Chisari FV (2006) Differential biophysical properties of infectious intracellular and secreted hepatitis C virus particles. J Virol 80: 11074-11081.

71. Yu X, Qiao M, Atanasov I, Hu Z, Kato T, et al. (2007) Cryo-electron microscopy and three-dimensional reconstructions of hepatitis C virus particles. Virology 367: 126-134.

72. Nielsen SU, Bassendine MF, Martin C, Lowther D, Purcell PJ, et al. (2008) Characterization of hepatitis C RNA-containing particles from human liver by density and size. J Gen Virol 89: 2507-2517.

73. Gastaminza P, Dryden KA, Boyd B, Wood MR, Law M, et al. (2010) Ultrastructural and biophysical characterization of hepatitis C virus particles produced in cell culture. J Virol 84: 10999-11009.

74. Catanese MT, Uryu K, Kopp M, Edwards TJ, Andrus L, et al. (2013) Ultrastructural analysis of hepatitis C virus particles. Proc Natl Acad Sci U S A 110: 9505-9510.

75. Seol Y, Skinner GM, Visscher K (2004) Elastic properties of a single-stranded charged homopolymeric ribonucleotide. Phys Rev Lett 93: 118102.

76. Seol Y, Skinner GM, Visscher K, Buhot A, Halperin A (2007) Stretching of homopolymeric RNA reveals single-stranded helices and base-stacking. Phys Rev Lett 98: 158103.

77. Safaee N, Noronha AM, Rodionov D, Kozlov G, Wilds CJ, et al. (2013) Structure of the parallel duplex of poly(A) RNA: evaluation of a 50 year-old prediction. Angew Chem Int Ed Engl 52: 10370-10373.

78. Arnott S, Chandrasekaran R, Marttila CM (1974) Structures for polyinosinic acid and polyguanylic acid. Biochem J 141: 537-543.

79. Kienberger F, Ebner A, Gruber HJ, Hinterdorfer P (2006) Molecular recognition imaging and force spectroscopy of single biomolecules. Acc Chem Res 39: 29-36.

80. Dufrêne YF, Hinterdorfer P (2008) Recent progress in AFM molecular recognition studies. Pflugers Arch 456: 237-245.

81. Hirano Y, Takahashi H, Kumeta M, Hizume K, Hirai Y, et al. (2008) Nuclear architecture and chromatin dynamics revealed by atomic force microscopy in combination with biochemistry and cell biology. Pflugers Arch 456: 139-153.

82. Takahashi H, Hizume K, Kumeta M, H Yoshimura S, Takeyasu K (2009) Single-molecule anatomy by atomic force microscopy and recognition imaging. Arch Histol Cytol 72: 217-225.

Citation: Gilmore JL, Aizaki H, Yoshida A, Deguchi K, Kumeta M, et al. (2014) Nanoimaging of ssRNA: Genome Architecture of the Hepatitis C Virus Revealed by Atomic Force Microscopy. J Nanomed Nanotechol S5: 010. doi:10.4172/2157-7439.S5-010

This article was originally published in a special issue, Nanotechnology: Challenges & Perspectives in Medicine handled by Editor(s). Dr. Malavosklish Bikram, University of Houston, USA

Organic LETTERS

Letter

pubs.acs.org/OrgLett

Isolation, Structure Elucidation, and Total Synthesis of Tryptopeptins A and B, New TGF-β Signaling Modulators from *Streptomyces* sp.

Yuta Tsunematsu,[†,‡] Shinichi Nishimura,[†] Akira Hattori,[†] Shinya Oishi,[§] Nobutaka Fujii,[§] and Hideaki Kakeya*[,†]

[†]Department of System Chemotherapy and Molecular Sciences and [§]Department of Bioorganic Medicinal Chemistry & Chemogenomics, Division of Bioinformatics and Chemical Genomics, Graduate School of Pharmaceutical Sciences, Kyoto University, Kyoto 606-8501, Japan

Supporting Information

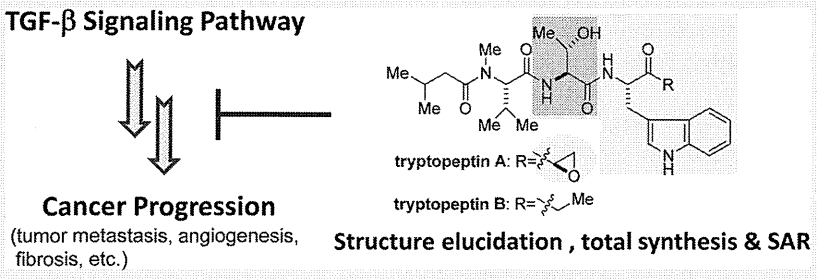

ABSTRACT: Two new microbial metabolites, tryptopeptins A (**1**) and B (**2**), were isolated from the cultured broth of *Streptomyces* sp. KUSC-G11, as modulators of the transforming growth factor-β (TGF-β) signaling pathway. Their chemical structures consisting of isovalerate, *N*-Me-L-Val, L-*allo*-Thr, and a tryptophan-related residue were elucidated on the basis of spectroscopic analyses, while they were unambiguously determined by total syntheses. A structure–activity relationship (SAR) study using natural and synthesized tryptopeptins revealed the importance of the α,β-epoxyketone function located at the *C* terminus. These new TGF-β signaling modulators would be highly useful for development of new drug leads targeting TGF-β-related diseases such as fibrosis and cancer.

Transforming growth factor-β (TGF-β) is a key molecule for cancer progression, since it facilitates cancer metastasis, organ fibrosis, angiogenesis and immunosuppression.[1] For example, epithelial–mesenchymal transition (EMT) induced by TGF-β is a crucial event in tumor metastasis; polarized and immotile epithelial cells differentiate into motile mesenchymal cells to be transferred to another organ via blood or lymph vessels. To combat cancer, small molecules inhibiting the TGF-β signaling pathway have been developed, some of which are under clinical trial.[2] However, most chemicals target TGF-β receptors, and a variety of chemicals with unique modes of action are requisite for exploring the therapeutic potential of modulation of TGF-β signaling. During the course of our screening for novel TGF-β modulators, we have found two novel microbial metabolites from *Streptomyces* sp. KUSC-G11, designated tryptopeptins A (**1**) and B (**2**). We herein describe the isolation, structure elucidation and total synthesis of tryptopeptins. The structure–activity relationship (SAR) is also discussed using natural and synthetic derivatives.

We conducted a cell-based screening against thousands of microbe culture extracts to find that the culture extract of *Streptomyces* sp. KUSC-G11 exhibited potent inhibitory activity against TGF-β signaling. Bioassay-guided fractionation by silica gel chromatography and repetitive reversed phase HPLC afforded novel metabolites **1** and **2** (Figure 1).

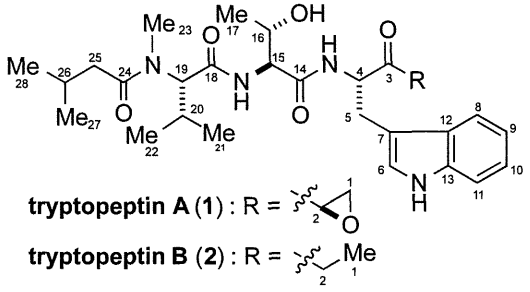

Figure 1. Structures of tryptopeptins A (**1**) and B (**2**).

Tryptopeptin A (**1**) was isolated as an optically active colorless oil ($[\alpha]_D^{27}$ = −94.3, *c* 0.010, MeOH). The molecular formula was determined to be $C_{28}H_{40}N_4O_6$ with 11 degrees of unsaturation, based on HR-FABMS (*m*/*z* 529.3028 $[M + H]^+$, Δ = +0.2 mmu, calcd. for $C_{28}H_{41}N_4O_6$, 529.3026) and 1D NMR spectra. Diagnostic signals in the NMR spectra indicated the peptidic nature of **1**; two amide protons (δ_H 7.12 and 6.78 ppm) and one *N*-methyl signal (δ_H 2.87 ppm) appeared in the ^{1}H NMR spectrum, while the ^{13}C NMR spectrum exhibited three amide carbonyl signals (δ_C 174.8, 171.6, and 171.1 ppm).

Received: November 18, 2014
Published: January 5, 2015

DOI: 10.1021/ol503340k
Org. Lett. 2015, 17, 258–261

2D NMR data including DQF-COSY, TOCSY, HSQC and HMBC spectra revealed the presence of one residue each of isovalerate, *N*-methylvaline (*N*-Me-Val) and threonine (Thr). The remaining portion was $C_{13}H_{13}N_2O_2$. Five aromatic proton signals (δ_H 7.62–7.08 ppm), one exchangeable NH signal (δ_H 9.17 ppm) and eight aromatic carbon signals (δ_C 137.5–110.2) indicated the presence of an indole ring, while a spin-system between an amide proton (4-NH), a methine proton (H-4) and methylene protons (H-5ab) was identified in the DQF-COSY spectrum, suggesting that **1** includes a tryptophan-related residue. The DQF-COSY and TOCSY spectra included another spin system consisting of one methine (H-2) and one methylene (H-1ab). The NMR signal that remains to be assigned was one carbonyl (C-3). HMBC correlations were observed from H-1, H-2, H-4 and H-5 to this carbon, indicating that the two spin systems H-1 to H-2 and 4-NH to H-5ab were connected through C-3 carbonyl. Finally, the unsaturation degree indicated the presence of an epoxide group, which was supported by characteristic chemical shift values for C-1 and C-2 (δ_C 47.7 and 53.0 ppm, respectively), deducing the structure of an α,β-epoxyketone functionality.

The sequence of amino acid residues was determined by interpretation of the HMBC data; the HMBC correlations from H-4, 4-NH and H-15 to C-14, from 15-NH and H-19 to C-18, and from H-19, H-23, H-25a and H-25b to C-24 allowed us to determine the sequence as follows: from *N*-terminus, isovalerate, *N*-Me-Val, Thr and *C*-terminally modified tryptophan-related residue possessing α,β-epoxyketone (Trp-EK) (Figure 2).

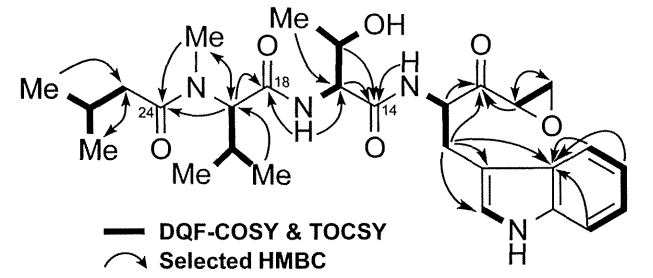

Figure 2. 2D NMR correlations in tryptopeptin A (**1**).

Tryptopeptin B (**2**) was obtained as a colorless oil ($[\alpha]_D^{25}$ = −96.0, *c* 0.010, MeOH). The molecular formula of $C_{28}H_{42}N_4O_5$, which was deduced by HR-ESIMS (*m/z* 537.3066 $[M + Na]^+$, Δ = +1.3 mmu, calcd. for $C_{28}H_{42}N_4NaO_5$, 537.3053), indicated loss of one oxygen atom and decrease of one degree of unsaturation when compared to the metabolite **1**. The ^1H and ^{13}C NMR spectra strongly suggested lack of an epoxide group. Instead, signals corresponding to an ethyl group (δ_H 0.89 and 2.45 ppm, and δ_C 7.6 and 33.7 ppm) were observed, indicating that the epoxyketone function of **1** was substituted by an ethyl ketone group. Detailed analysis of the 2D NMR data confirmed the presence of the ethyl ketone group, and we could determine the planar structure of **2** as depicted in Figure 1.

We next tried to determine the stereochemistry of tryptopeptins. The advanced Marfey's method[3] was applied to determine the absolute configuration of amino acids. The acid hydrolysate of **2** was condensed with Marfey's reagents L- or D-FDLA, and the products were analyzed by LC–MS. L-FDLA derivative of *N*-Me-valine was eluted faster than the D-FDLA derivative on reversed phase HPLC, which indicated the presence of *N*-Me-L-Val[3] in **2**. The configuration of Thr was determined to be L-*allo*-Thr by comparing the retention times with those of FDLA-derivatized authentic Thr and *allo*-Thr (Figure S15, Supporting Information). Unfortunately, however, we could not determine the configuration of C-4 since FDLA derivatives of the tryptophan-related residue were not detected. By contrast, the configuration of the Trp-EK in metabolite **1** was only speculatively deduced by the NMR analysis (Figure S14). To determine the absolute configuration of these tryptopeptins, we conducted the total synthesis of tryptopeptins.

Tryptopeptin A (**1**) seems to have the same configuration to that of **2**; these two molecules shared the same amino acid backbone, suggesting that they are biosynthesized by a common nonribosomal peptide synthetase (NRPS) machinery. In addition, they exhibited very similar ^1H NMR signals especially for the backbone protons. Retrosynthetic analysis of tryptopeptins **1** and **2** is shown in Scheme 1. We planned to

Scheme 1. Retrosynthetic Analysis of Four and Two Possible Diastereomers of Tryptopeptins A (1a–1d) and B (2a and 2b), Respectively

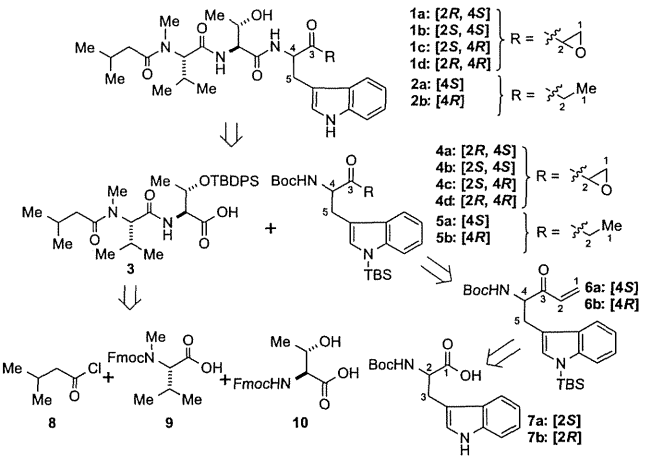

synthesize them by conjugating the corresponding *N*-terminal and *C*-terminal fragments; **1** could be synthesized with **3** and **4**, and **2** from **3** and **5**, respectively. The common segment **3** consisting of isovalerate, *N*-Me-L-Val and L-*allo*-Thr could be obtained by a conventional peptide synthesis methodology from **8**–**10**. In contrast, we had to synthesize a set of stereoisomers of the *C*-teminal fragment for determining the configuration of the natural products. We expected that four diastereomers **4a**–**4d** could be obtained by epoxidation of an α,β-enone **6a** or **6b** (**6a** and **6b** with 4*S* and 4*R* configuration, respectively), while another set of two diastereomers **5a** and **5b** could be synthesized by reduction of **6a** and **6b**, respectively. The α,β-enones **6a** and **6b** could be synthesized from commercially available *N*-Boc-L-tryptophan **7a** and its enantiomer **7b**, respectively.

We began the synthetic work by preparing chiral tryptophan-related residues (Scheme 2A). We first synthesized **6a**, a common intermediate for **4a**, **4b** and **5a**. *N*-Boc-L-Trp **7a** was converted to Weinreb's amide,[4] followed by protection of the indole nitrogen with a TBS group to afford **11**. Grignard reaction of **11** with vinylmagnesium chloride gave the corresponding enone **6a**. We next tried to synthesize epoxyketone **4a** and **4b** from **6a**. We first attempted Sharpless asymmetric epoxidation or dihydroxylation to an allylic alchol

DOI: 10.1021/ol503340k
Org. Lett. 2015, 17, 258–261

Scheme 2. Syntheses of Tryptopeptin A (1a–1d) and B (2a and 2b) Diastereomers[a]

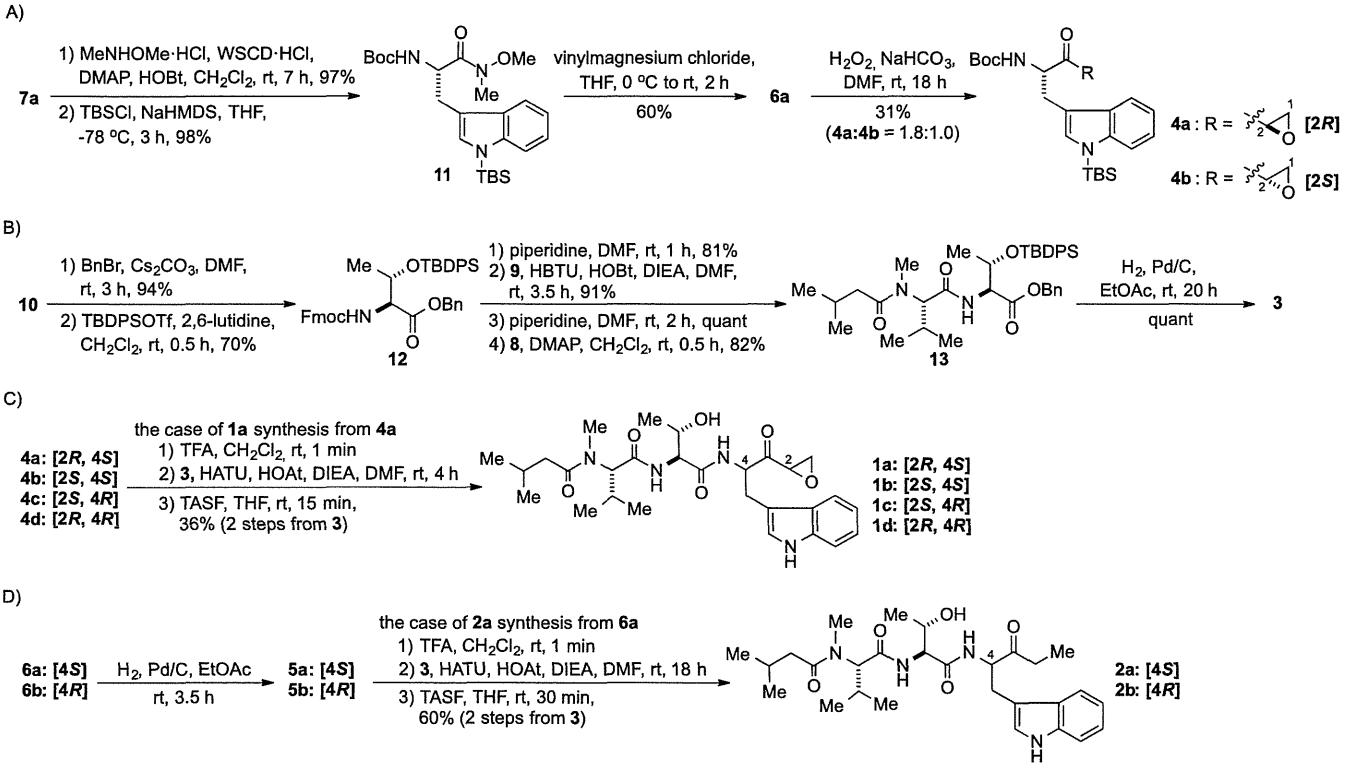

[a](A) Syntheses of tryptopeptin A *C*-terminal fragments **4a** and **4b**. (B) Common *N*-terminal fragment synthesis. (C) Syntheses of tryptopeptin A diastereomers (**1a–1d**). (D) Syntheses of tryptopeptin B diastereomers (**2a** and **2b**).

derivative that was prepared from **6a** with $NaBH_4$; however, these strategies were not satisfactory due to the low reaction yields. We then tested a nonstereoselective route, which can conveniently furnish diastereomers. After testing several epoxidation conditions, we found that treatment of enone **6a** with $H_2O_2/NaHCO_3$ afforded diastereomers of α,β-epoxyketones **4a** and **4b** (31%, **4a**:**4b** = 1.8:1.0). We purely separated two products by reversed phase HPLC. The absolute configuration of the epoxide (C2-position) was determined by derivatization and spectroscopic analysis (Scheme S2, Figures S16–S17). Another set of diastereomers **4c** and **4d** were prepared from **7b** in a similar fashion (Scheme S3). On the other hand, hydrogenation of **6a** successfully furnished the ethyl ketone residue **5a**, in addition, the enantiomer **5b** was prepared from **6b** (Scheme 2D).

The *N*-terminal fragment was constructed by applying conventional Fmoc chemistry (Scheme 2B). Fmoc-protected L-*allo*-Thr (**10**) was converted to the benzyl ester and its secondary hydroxyl group was protected by the TBDPS group to give **12**. After removal of the Fmoc group, *allo*-Thr was coupled with **9**, followed by Fmoc deprotection and acylation with **8**, which afforded the acylated dipeptide **13**. Subsequent removal of the benzyl ester by hydrogenation yielded the *N*-terminal fragment **3**.

Synthesis of tryptopeptins was accomplished by conjugation of the corresponding *C*-terminal and *N*-terminal fragments followed by deprotection. To obtain four possible diastereomers of **1**, the *N*-terminal fragment **3** and the *C*-termical fragments derived from **4** were condensed; *C*-terminal fragments (**4a**, **4b**, **4c** or **4d**) were deprotected with TFA[5] and immediately coupled with the *N*-terminal fragment **3** using HATU. Finally, we carefully deprotected the secondary alcohol with TASF to afford the four diastereomers **1a–1d**, respectively[6] (Scheme 2C, Scheme S4). With four possible diastereomers of natural tryptopeptin A (**1**) in hand, we compared their physicochemical properties including NMR spectra to that of the natural one. We found that only synthetic **1a** exhibited similar properties to those of natural **1** (Table S3, Figures S19–S22, S55); for example, optical rotation values of natural **1** and synthetic **1a** were close (**1**: $[\alpha]_D^{27}$ = −94.3, *c* 0.010, MeOH, **1a**: $[\alpha]_D^{27}$ = −96.9, *c* 0.064, **1b**: $[\alpha]_D^{26}$ = −157.2, *c* 0.25, MeOH, **1c**: $[\alpha]_D^{26}$ = −127.1, *c* 0.25, MeOH, **1d**: $[\alpha]_D^{25}$ = −50.3, *c* 0.25, MeOH). Thus, we concluded that the natural product **1** consists of isovalerate, *N*-Me-L-Val, L-*allo*-Thr and a tryptophan-related residue (Trp-EK) with 2*R*,4*S* configurations.

Two possible diastereomers of tryptopeptin B (**2**) were synthesized from the *C*-terminal fragment **5a** or **5b** and the *N*-terminal **3** in a similar way as described above; *N*-Boc deprotection, peptide condensation and silyl-deprotection afforded **2a** and **2b**, respectively (Scheme 2D). We compared their physicochemical properties and found that **2a**, not **2b**, exhibited similar properties to those of natural **2** (Table S4, Figures S23–S27 and S56), concluding the configuration of 4*S*. As predicted above, tryptopeptins **1** and **2** shared common absolute configurations.

With two natural and six synthesized tryptopeptins in hand, SAR study was conducted. Among compounds tested, tryptopeptin A (**1**) showed the most potent inhibitory activity with the IC_{50} of 1.0 μM against TGF-β signaling without cytotoxicity (Figure 3 and S57). It is noteworthy that a loss of an epoxide moiety of tryptopeptins caused a significant decrease in the TGF-β inhibitory activities; the IC_{50} values for **2** and **2b** are 55 and 70 μM, respectively. We also found that

DOI: 10.1021/ol503340k
Org. Lett. 2015, 17, 258–261

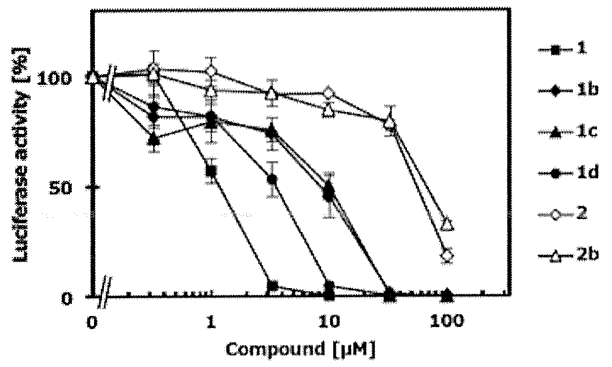

Figure 3. TGF-β signaling inhibitory activities of tryptopeptin A (**1**), tryptopeptin B (**2**) and their synthetic diastereomers (**1b**–**1d** and **2b**).

the configuration of the epoxide group affected the inhibitory activity; the IC_{50} values of **1**, **1b**, **1c**, and **1d** were 1.0, 8.0, 10.0, and 3.2 μM, respectively, indicating that the diastereomers with 2*S* configuration exhibited weaker inhibition than the compounds with 2*R* configuration (Figure 3). Similar tendency was observed in the growth inhibitory activities against HeLa cells (Figure S58). Importantly, natural tryptopeptins (**1** and **2**) and synthetic tryptopeptins with the same configuration (**1a** and **2a**) exhibited the same biological activities (Figures S55 and S56), which also confirmed the absolute configuration of the natural tryptopeptins. Taken together, tryptopeptin A (**1**) with 2*R*,4*S* configurations exhibited the most potent biological activities, suggesting that target molecule(s) in a cell might recognize the configurations of the epoxyketone.

So far, several compounds possessing a peptidyl α,β-epoxyketone function have been reported from microorganisms, e.g., histone deacetylase inhibitor trapoxins,[7] and 20*S* proteasome inihibitors epoxomicin[8a] and eponemycins.[8b] The α,β-epoxyketone group has been revealed to play a crucial role in the enzyme inhibition, by forming a covalent bond with the catalytic residue in the enzyme.[9] In this study, we showed the presence and the absolute configuration of epoxide in tryptopeptins affected the potency of TGF-β signaling inhibition. It is likely that we can fish the cellular targets taking advantage of the reactivity of the epoxyketone group. Synthesis and evaluation of tryptopeptin probes are under way in our laboratory.

Tryptopeptins consist of four blocks; among them, L-*allo*-Thr is a rare residue in nature, while there is no report on the *C*-terminally modified tryptophan-related residue. The peptide backbones might be constructed by NRPS and *C*-terminus of L-tryptophan is likely elongated by polyketide synthase (PKS), followed by some modifications to form α,β-epoxyketone group in compound **1**. Recently, the biosynthetic gene clusters of epoxomicin and eponemycin were reported, whereas the mechanism of the *C*-terminus modification is unknown.[10] Genomic sequencing of the tryptopeptin producer *Streptomyces* sp. KUSC-G11 would unveil the biosynthetic mechanism of tryptopeptins including generation of the Trp-EK.

In summary, we isolated two novel natural products, tryptopeptins A (**1**) and B (**2**), from the cultured broth of *Streptomyces* sp. as TGF-β signaling inhibitors. Chemical structures were unambiguously determined by spectroscopic analyses and total syntheses. Since TGF-β signaling is deeply involved in cancer progression, understanding modes of action of tryptopeptins would open a way for cancer chemotherapy.

■ ASSOCIATED CONTENT

Ⓢ Supporting Information

Experimental procedures, compound data, tables of NMR data, 1D and 2D NMR spectra, and results of biological assays. This material is available free of charge via the Internet at http://pubs.acs.org.

■ AUTHOR INFORMATION

Corresponding Author

*E-mail: scseigyo-hisyo@pharm.kyoto-u.ac.jp.

Present Address

‡Department of Pharmaceutical Sciences, University of Shizuoka, Shizuoka 422-8526, Japan.

Notes

The authors declare no competing financial interest.

■ ACKNOWLEDGMENTS

We thank Dr. Kojima, S. (RIKEN Institute) and Morioka, M. (Kyoto University) for providing a p(CAGA)$_9$MLP-Luc reporter plasmid and supporting biological assay, respectively. We are grateful to Dr. Takasu, Y., Dr. Sakai, Y., Hayashi, R. and Dr. Inokuchi, E. (Kyoto University) for helpful discussions on organic synthesis. Y.T. is grateful for assistance from JSPS research fellowships for young scientist. This work was supported in part by research grants from the Japan Society for the Promotion of Science (JSPS), the Ministry of Education, Culture, Sports, Science and Technology of Japan (MEXT), the Ministry of Health, Labor and Welfare of Japan (MHLW), and SRF.

■ REFERENCES

(1) Miyazono, K. *Proc. Jpn. Acad., Ser. B* **2009**, *85*, 314–323.

(2) Nagaraj, N. S.; Datta, P. K. *Expert Opin. Invest. Drugs* **2010**, *19*, 77–91.

(3) (a) Marfey, P. *Carlsberg Res. Commun.* **1984**, *49*, 591–596. (b) Fujii, K.; Ikai, Y.; Oka, H.; Suzuki, M.; Harada, K. *Anal. Chem.* **1997**, *69*, 3346–3352. (c) Fujii, K.; Ikai, Y.; Oka, H.; Suzuki, M.; Harada, K. *Anal. Chem.* **1997**, *69*, 5146–5151.

(4) Nahm, S.; Weinreb, S. M. *Tetrahedron Lett.* **1981**, *22*, 3815–3818.

(5) Sin, N.; Kim, K. B.; Elofsson, M.; Meng, L. H.; Auth, H.; Kwok, B. H. B.; Crews, C. M. *Bioorg. Med. Chem. Lett.* **1999**, *9*, 2283–2288.

(6) Although we tried several desilylating conditions, only TASF gave the desired product. In other conditions, only degradation of the starting material was observed.

(7) Itazaki, H.; Nagashima, K.; Sugita, K.; Yoshida, H.; Kawamura, Y.; Yasuda, Y.; Matsumoto, K.; Ishii, K.; Uotani, N.; Nakai, H.; Terui, A.; Yoshimatsu, S.; Ikenishi, Y.; Nakagawa, Y. *J. Antibiot.* **1990**, *43*, 1524–1532.

(8) (a) Hanada, M.; Sugawara, K.; Kaneta, K.; Toda, S.; Nishiyama, Y.; Tomita, K.; Yamamoto, H.; Konishi, M.; Oki, T. *J. Antibiot.* **1992**, *45*, 1746–1752. (b) Sugawara, K.; Hatori, M.; Nishiyama, Y.; Tomita, K.; Kamei, H.; Konishi, M.; Oki, T. *J. Antibiot.* **1990**, *43*, 8–18.

(9) Groll, M.; Kim, K. B.; Kairies, N.; Huber, R.; Crews, C. M. *J. Am. Chem. Soc.* **2000**, *122*, 1237–1238.

(10) Schorn, M.; Zettler, J.; Noel, J. P.; Dorrestein, P. C.; Moore, B. S.; Kaysser, L. *ACS Chem. Biol.* **2013**, *9*, 301–309.

DOI: 10.1021/ol503340k
Org. Lett. 2015, 17, 258–261

CellPress

Chemistry & Biology
Article

Balance between Exocytosis and Endocytosis Determines the Efficacy of Sterol-Targeting Antibiotics

Shinichi Nishimura,[1,*] Masato Tokukura,[1] Junko Ochi,[1] Minoru Yoshida,[2] and Hideaki Kakeya[1,*]
[1]Division of Bioinformatics and Chemical Genomics, Department of System Chemotherapy and Molecular Sciences, Graduate School of Pharmaceutical Sciences, Kyoto University, Kyoto 606-8501, Japan
[2]Chemical Genomics Research Group, RIKEN Center for Sustainable Resource Science, Wako, Saitama 351-0198, Japan
*Correspondence: nshin@pharm.kyoto-u.ac.jp (S.N.), scseigyo-hisyo@pharm.kyoto-u.ac.jp (H.K.)
http://dx.doi.org/10.1016/j.chembiol.2014.10.014

SUMMARY

Antifungals targeting membrane ergosterol are longstanding, yet indispensable drugs in clinical use. However, the mechanisms by which the cellular membrane domains recognized by these antibiotics are generated remain largely unknown. Here, we demonstrate that the balance between endocytosis and exocytosis in membrane trafficking is a critical factor in the action of sterol-targeting antibiotics. When fission yeast cells were treated with manumycin A, cellular binding and the action of the antifungals filipin, amphotericin B, and theonellamides, all of which are ergosterol-binders, were abolished. Additionally, manumycin A treatment attenuated Cdc42 activity and inhibited exocytosis, while endocytosis was only moderately suppressed. Similar defects in membrane trafficking could be reproduced by heat shock and genetic perturbation, which also abolished the action of the antibiotics. We propose that exocytosis and endocytosis respectively supply and internalize the specific plasma membrane domains recognized by sterol-targeting antibiotics.

INTRODUCTION

The cell membrane serves as a physical barrier that defines the cell boundary and segregates the interior into distinct compartments, each performing a specialized function. Among the many lipid constituents of cell membranes, sterols are unique in that they are major regulators of membrane fluidity and thickness and contribute to the formation of specific membrane microdomains (Simons and Ikonen, 1997). Additionally, sterols are medically important molecules often targeted by antibiotics and toxins. Using artificial membranes, many studies have been carried out to gain insights into the action of sterol-targeting exogenous molecules. However, as yet, little is known about how antibiotics recognize the cellular membrane, and how the corresponding membrane domains are generated in the cell (Bolard, 1986; Gray et al., 2012). Cellular membranes are highly complex; it is therefore imperative to use the right model organism with clear-cut phenotypes to elucidate the basic mechanisms behind the construction of the living cell membrane.

The fission yeast *Schizosaccharomyces pombe* is a rod-shaped unicellular organism that grows by length extension at the cell tips, where actin patches, glucan synthases, and the processes of exocytosis and endocytosis are all concentrated (Hayles and Nurse, 2001). Sterol-rich domains in the plasma membrane have also been detected at the growing cell tips (Wachtler et al., 2003). Most of the components located at the cell tips during interphase, including these sterol-rich plasma membrane domains, are recruited to the site of cytokinesis for equal distribution upon cell division. Since the polarity of sterol-rich membrane domains in *S. pombe* cells can be clearly visualized using sterol probes and fluorescence microscopy (Nishimura et al., 2010; Wachtler et al., 2003), *S. pombe* is an excellent model organism for investigating the physical and biological nature of sterol-rich membrane domains. The polarized distribution of these domains is regulated in a cell cycle-dependent manner (Wachtler et al., 2003) and has been shown to require normal actin cytoskeleton organization (Codlin et al., 2008; Takeda et al., 2004), myosin type I (Myo1) protein (Takeda and Chang, 2005), and Cdc15, a contractile ring protein (Takeda et al., 2004).

In addition to the cytoskeletal machinery, the functional secretory pathway was also shown to be necessary for sterol-rich membrane domain distribution; in cell-cycle mutant *cdc25-22* cells, brefeldin A (BFA), an inhibitor of ER-to-Golgi transport (Graham et al., 1993), inhibited the appearance of sterol-rich domains (Wachtler et al., 2003). However, in wild-type cells, BFA treatment yielded rather bright fluorescent signals that lost polarity, raising the question of whether the functional secretory pathway alone is sufficient for generating polarized sterol localization (Figure S1A available online).

During the course of screening for chemical modulators of the action of membrane-targeting antibiotics, we found that manumycin A (manu-A) inhibited the binding of sterol-targeting antibiotics to fission yeast cells. Here, using manu-A as a chemical genetics tool, we demonstrate that the balance between exocytosis and endocytosis is critical for generating the membrane domains recognized by sterol-targeting antibiotics.

RESULTS AND DISCUSSION

Manu-A Abolishes the Cellular Binding of Sterol-Targeting Antibiotics

Sterol-rich domains in the plasma membrane can be visualized with filipin, a polyene antibiotic that exhibits fluorescence upon binding to membrane sterols (Drabikowski et al., 1973). To investigate how cellular membranes are recognized by sterol-targeting antibiotics, we tested a set of chemicals for their effect on filipin staining. We found that when cells were pretreated with manu-A (see structure in Figure 1A), the fluorescent signal from filipin was absent (Figure 1B). There are two possible mechanisms for this phenomenon: manu-A might quench the fluorescence of the filipin-sterol complexes, or it might sequester sterols, thereby hampering the formation of the filipin-sterol complexes. To investigate these possibilities, we tested the effect of manu-A on other sterol-targeting antibiotics. First, we tested amphotericin B (AmB), another polyene antibiotic that is commonly prescribed as an ergosterol-targeting antifungal drug (Volmer et al., 2010). AmB is known to induce large vacuoles in yeast cells, probably as a consequence of binding to ergosterol (Bhuiyan et al., 1999). However, this morphological change was suppressed when the cells were pretreated with manu-A (Figure 1C). Notably, the toxicity of filipin and AmB were also attenuated (Figure 1D). In fission yeast cells, filipin showed toxicity at 2 μg/ml and partially inhibited growth of the cells at 1 μg/ml. In the presence of manu-A, growth inhibition by filipin (1 μg/ml) was not observed, although it must be noted that cell growth was attenuated by manu-A across all filipin concentrations. The mitigating effect of manu-A on AmB toxicity was more distinct, as the minimum inhibitory concentration (MIC value) of AmB doubled in the presence of manu-A.

Next, we examined theonellamides (TNMs), bicyclic peptides isolated from marine sponges (Matsunaga and Fusetani, 1995; Matsunaga et al., 1989) that target membrane sterols (Espiritu et al., 2013). TNM fluorescent derivatives, such as TNM-aminomethylcoumarin acetate (AMCA), specifically recognize 3β-hydroxysterols. These fluorescent derivatives can therefore act as markers of 3β-hydroxysterols in both yeast (Ho et al., 2009; Nishimura et al., 2010) and cultured mammalian cells (Nishimura et al., 2013). TNM-AMCA treatment of the fission yeast cells exhibited polarized staining similar to that obtained with filipin, and this staining was also inhibited by pretreatment with manu-A (Figure 1E). Treatment of fission yeast cells with TNMs induces abnormal cell wall morphology (Nishimura et al., 2010). Consistent with the inhibition of the cellular binding of TNM-AMCA by manu-A, this abnormal cell wall phenotype was not observed following pretreatment with manu-A (data not shown). Additionally, growth inhibition by TNM-A was also attenuated (Figure 1D), and manu-A quadrupled the MIC value of this compound. Because filipin, AmB, and TNMs belong to different chemical classes based on their structure (Figure S2), the effect of manu-A is unlikely to be dependent on the chemical properties of the antibiotics. It is unlikely that the fluorescence of the filipin-sterol complexes was directly quenched by manu-A. Instead, it is likely that manu-A treatment sequesters antibiotic-targeted ergosterol molecules in the plasma membrane using as yet unknown mechanisms.

Manu-A was originally isolated from *Streptomyces parvulus* (Zeeck et al., 1987). This metabolite has been reported to inhibit several enzymes including caspase I (Tanaka et al., 1996) and neutral sphingomyelinase (Arenz et al., 2001), and protein farnesyltransferase (FTase) (Hara et al., 1993). It has also been observed to inhibit protein FTase in the budding yeast, *Saccharomyces cerevisiae* (Hara et al., 1993). We therefore examined the possibility that FTase inhibition is responsible for the effects of manu-A observed in *S. pombe*. Protein FTase consists of α and β subunits encoded by the *cwp1* and *cpp1* genes, respectively. FTase activity was abolished in cells lacking the *cpp1* gene (Yang et al., 2000), however, sterol-rich membrane domains were still observed to localize in a polarized manner, although polarity in the cell shape was severely reduced (Figure 1F) (Ma et al., 2006). Additionally, the sterol-rich domains of these mutant cells disappeared after treatment with manu-A. We also examined the *css1* gene, which encodes inositol phosphosphingolipid phospholipase C, a yeast counterpart of mammalian sphingomyelinase. Manu-A has been reported to inhibit neutral sphingomyelinase (Arenz et al., 2001). Sphingomyelinase catalyzes the hydrolysis of sphingomyelin to produce ceramide, which is required for membrane budding in liposomes and exocytosis in mammalian cells (Trajkovic et al., 2008). However, *css1* mutant cells did not reproduce the phenotype of manu-A treatment (Figure S3A). These results indicated that protein FTase and inositol phosphosphingolipid phospholipase C do not mediate the effect of manu-A on the plasma membrane.

Sterol Levels and Sterol-Rich Membrane Domains

The disappearance of sterol-rich domains from the plasma membrane can be caused by a decrease in sterol levels. We therefore measured the amount of ergosterol present in cells subsequent to treatment with manu-A, under the following two conditions. When cells were cultivated in a rich medium containing manu-A (1 μg/ml), the ergosterol level decreased to 77.7 ± 6.0% and no filipin signal was detected (Figure 1B). In contrast, when cells were cultivated in a synthetic medium, a lower concentration of manu-A (0.1 μg/ml) decreased the ergosterol level to a similar level of 75.6 ± 2.7%, although the filipin signal was still observed (Figure S3B). These results revealed that the amount of ergosterol present could not be correlated to the presence or absence of sterol-rich domains in the plasma membrane. We next compared the kinetics of the effect of manu-A and terbinafine, a potent inhibitor of squalene epoxidase, a requisite enzyme for ergosterol biosynthesis (Figures S3C and S3D). Compared with manu-A, a longer incubation period (more than 5 h) with terbinafine was required before the sterol-rich membrane domains were observed to disappear. These results suggested that a decrease in ergosterol was not responsible for the disappearance of sterol-rich membrane domains in the presence of manu-A. The decreased ergosterol levels affected by manu-A may be a result of feedback regulation following dysregulation of membrane trafficking (as discussed further below). As a case in point, cells lacking the *apm1* gene, which encodes the AP-1 adaptor complex μ subunit involved in vesicle-mediated transport, are known to contain only about 50% of ergosterol due to an unknown mechanism (Fang et al., 2012).